

## **INFORMATION TO USERS**

**This manuscript has been reproduced from the microfilm master. UMI films the text directly from the original or copy submitted. Thus, some thesis and dissertation copies are in typewriter face, while others may be from any type of computer printer.**

**The quality of this reproduction is dependent upon the quality of the copy submitted. Broken or indistinct print, colored or poor quality illustrations and photographs, print bleedthrough, substandard margins, and improper alignment can adversely affect reproduction.**

**In the unlikely event that the author did not send UMI a complete manuscript and there are missing pages, these will be noted. Also, if unauthorized copyright material had to be removed, a note will indicate the deletion.**

**Oversize materials (e.g., maps, drawings, charts) are reproduced by sectioning the original, beginning at the upper left-hand corner and continuing from left to right in equal sections with small overlaps.**

**Photographs included in the original manuscript have been reproduced xerographically in this copy. Higher quality 6" x 9" black and white photographic prints are available for any photographs or illustrations appearing in this copy for an additional charge. Contact UMI directly to order.**

**Bell & Howell Information and Learning  
300 North Zeeb Road, Ann Arbor, MI 48106-1346 USA**

**UMI<sup>®</sup>**  
**800-521-0600**



Study of Charmonium Final States in  $B$  Meson  
Decays

Tarek Saab  
Department of Physics  
McGill University  
Montréal, Québec  
Canada

February 6, 1998

A thesis submitted to the  
Faculty of Graduate Studies and Research  
in partial fulfillment of  
the requirements for the degree of  
Master of Science

©Tarek Saab, 1998



National Library  
of Canada

Acquisitions and  
Bibliographic Services

395 Wellington Street  
Ottawa ON K1A 0N4  
Canada

Bibliothèque nationale  
du Canada

Acquisitions et  
services bibliographiques

395, rue Wellington  
Ottawa ON K1A 0N4  
Canada

*Your file* *Votre référence*

*Our file* *Notre référence*

The author has granted a non-exclusive licence allowing the National Library of Canada to reproduce, loan, distribute or sell copies of this thesis in microform, paper or electronic formats.

The author retains ownership of the copyright in this thesis. Neither the thesis nor substantial extracts from it may be printed or otherwise reproduced without the author's permission.

L'auteur a accordé une licence non exclusive permettant à la Bibliothèque nationale du Canada de reproduire, prêter, distribuer ou vendre des copies de cette thèse sous la forme de microfiche/film, de reproduction sur papier ou sur format électronique.

L'auteur conserve la propriété du droit d'auteur qui protège cette thèse. Ni la thèse ni des extraits substantiels de celle-ci ne doivent être imprimés ou autrement reproduits sans son autorisation.

0-612-44266-7

Canada

**This work is dedicated to the McGill physics class of 1995.**

## Abstract

$B^\pm$  mesons are reconstructed via two decay modes:  $B^\pm \rightarrow \chi_c K^\pm$  and  $B^\pm \rightarrow J/\psi K^\pm$  from data collected by the CDF experiment, corresponding to an integrated luminosity of  $109 \text{ pb}^{-1}$ . An unambiguous  $B^\pm \rightarrow J/\psi K^\pm$  signal is observed; however, the  $B^\pm \rightarrow \chi_c K^\pm$  signal was not of sufficient quality to allow for the determination of the relative branching ratios of the two processes.

## Résumé

Nous reconstruisons les mésons  $B^\pm$  pour les deux modes de désintégration  $B^\pm \rightarrow \chi_c K^\pm$  et  $B^\pm \rightarrow J/\psi K^\pm$  à partir de données prises lors de l'expérience CDF, pour une luminosité intégrée de  $109 \text{ pb}^{-1}$ . Nous observons un signal clair pour la réaction  $B^\pm \rightarrow J/\psi K^\pm$ , mais le signal de la réaction  $B^\pm \rightarrow \chi_c K^\pm$  est beaucoup plus faible. Par conséquent, nous ne pouvons déterminer le rapport de branchement relatif de ces deux processus de désintégration.

## Acknowledgements

I extend my greatest thanks to my supervisor Ken Ragan for giving me the opportunity to work with an ongoing high energy physics experiment and for providing help and guidance throughout my graduate studies. I would also like to thank my colleagues and friends, both within the physics department and the CDF group for helping to make graduate work less of a chore and more of a pleasure. Particular thanks are directed to Kostas Kordas for helping me in getting started with my research and for help throughout my studies. I am also extremely grateful to Klaus Strahl, whose infinite patience and periodic pastries managed to get some work out of me.

Last but not least, I would like to thank my family and my brother for being very supportive throughout my studies and especially during the last few months of thesis writing. I hope that the rest of my career in physics and academia will be as pleasurable and enriching as this experience has been.

This work was supported by Natural Sciences and Engineering Research Council of Canada to whom I am also very thankful.

# Contents

<b>Abstract</b>	<b>ii</b>
<b>Résumé</b>	<b>iii</b>
<b>Acknowledgements</b>	<b>iv</b>
<b>1 Introduction</b>	<b>1</b>
<b>2 <math>B</math> physics at CDF</b>	<b>7</b>
<b>3 The CDF Detector</b>	<b>12</b>
3.1 Introduction . . . . .	12
3.1.1 The Silicon Vertex Detector . . . . .	15
3.1.2 The Central Tracking Chamber . . . . .	17
3.1.3 The Central Calorimeters . . . . .	20
3.1.4 The Muon Chambers . . . . .	23
3.2 The CDF Trigger . . . . .	27
3.3 Event Structure . . . . .	29
<b>4 The <math>B^\pm</math> Signal</b>	<b>32</b>

4.1	Reconstruction Strategy . . . . .	35
4.1.1	Calculation of Invariant Masses . . . . .	35
4.1.2	Reconstruction of the Decay Chains . . . . .	36
4.2	Selection Criteria . . . . .	38
4.2.1	Muon Selection . . . . .	39
4.2.2	$J/\psi$ Reconstruction . . . . .	40
4.2.3	$K^\pm$ Selection . . . . .	42
4.2.4	$B^\pm \rightarrow J/\psi K^\pm$ Reconstruction . . . . .	43
4.2.5	$\gamma$ Selection . . . . .	44
4.2.6	$\chi_c$ Reconstruction . . . . .	45
4.2.7	$B^\pm \rightarrow \chi_c K^\pm$ Reconstruction . . . . .	47
4.3	Summary of Reconstructed Decays . . . . .	48
<b>5</b>	<b>Relative Reconstruction Efficiency of the <math>B^\pm</math> Decay Modes</b>	<b>52</b>
5.1	The Monte Carlo Simulation . . . . .	53
5.2	$B^\pm$ Reconstruction Efficiencies . . . . .	54
5.2.1	The $P_T(K^\pm)$ Cut Efficiency . . . . .	57
5.2.2	The $P_T(\mu)$ Cut and the Trigger Efficiency . . . . .	59
5.2.3	The $P_T(J/\psi)$ Cut . . . . .	60
5.3	The Photon Reconstruction Efficiency . . . . .	63
5.3.1	The Conversion electrons . . . . .	64

5.3.2	Determination of the Photon Reconstruction Efficiency	66
5.3.3	The 'No Track Cut' Efficiency . . . . .	66
5.3.4	The 'Photon Fiducial Volume Cut' Efficiency . . . . .	68
5.4	The Total Relative Efficiency . . . . .	68
5.5	Systematic Errors . . . . .	69
<b>6</b>	<b>Results and Conclusions</b>	<b>70</b>

# List of Figures

2.1	Illustration of the Tevatron main storage and acceleration rings.	7
2.2	Feynman diagram of the $b$ quark decay.	9
2.3	Feynman diagram of the $B^-$ meson decays $B^- \rightarrow J/\psi K^-$ and $B^- \rightarrow \chi_c K^-$ .	10
2.4	Feynman diagram of the $J/\psi$ meson decay into $\mu^+\mu^-$ .	11
2.5	Feynman diagram of the $\chi_c$ meson decay into $\mu^+\mu^-\gamma$ .	11
3.1	Schematic drawing of the CDF detector.	13
3.2	A cross-sectional view of the SVX.	16
3.3	An end view of the CTC endplate.	18
3.4	An illustration of the CEM towers in a calorimeter wedge.	21
3.5	Schematic of the regions covered by each of the CMU, CMP, and CMX in $\eta - \phi$ space.	24
3.6	Schematic of the muon chamber wedges.	25
3.7	Illustration of the sense wire configuration in a CMU muon tower.	26

4.1	The $\chi_x^2$ distribution of the muon candidates in the Run 1A data. The $\chi^2$ distribution of the Run 1B data is similar to this. The arrow denoted the value of the $\chi_x^2$ cut. . . . .	39
4.2	The $\chi_z^2$ distribution of the muon candidates in the Run 1A data. The $\chi^2$ distribution of the Run 1B data is similar to this. The arrow denoted the value of the $\chi_z^2$ cut. . . . .	40
4.3	The $P_T$ spectrum of the muons in the total data sample. . . . .	41
4.4	The invariant mass distribution of the $J/\psi$ candidates. . . . .	42
4.5	The $J/\psi K^\pm$ invariant mass distribution. . . . .	45
4.6	The $P_T(J/\psi K^\pm)$ distribution. . . . .	46
4.7	The $\chi_c$ candidate mass spectrum. . . . .	47
4.8	The invariant $\chi_c K^\pm$ mass distribution. . . . .	49
4.9	The $P_T$ of the $B$ candidates. . . . .	50
5.1	The Monte Carlo generated $B^\pm P_T$ spectrum. . . . .	58
5.2	The Monte Carlo $P_T$ spectra of the $K^\pm$ from $B^\pm$ decay. . . . .	58
5.3	$P_T$ spectra of the $B^\pm$ with the $K^\pm P_T$ cuts. . . . .	59
5.4	Efficiency of the $K^\pm P_T$ cut, for the $B^\pm \rightarrow \chi_c K^\pm$ decay mode with respect to the $B^\pm \rightarrow J/\psi K^\pm$ decay mode, as a function of $B^\pm P_T$ . . . . .	59
5.5	The Monte Carlo $P_T$ spectra of the more energetic muon from the $B^\pm$ decay. . . . .	60

5.6	The Monte Carlo $P_T$ spectra of the less energetic muon from the $B^\pm$ decay. . . . .	61
5.7	$P_T$ spectra of the $B^\pm$ with the muon $P_T$ cuts. . . . .	61
5.8	Efficiency of the muon $P_T$ cuts, for the $B^\pm \rightarrow \chi_c K^\pm$ decay mode with respect to the $B^\pm \rightarrow J/\psi K^\pm$ decay mode, as a function of $B^\pm P_T$ . . . . .	62
5.9	The Monte Carlo $P_T$ spectra of the $J/\psi$ from the $B^\pm$ decay. . . . .	62
5.10	Efficiency of the $J/\psi$ $P_T$ cuts, after the muon $P_T$ have been imposed, as a function of $B^\pm P_T$ . . . . .	63
5.11	Radial distribution of the conversion vertices in the $r - \phi$ plane. . . . .	65
5.12	Energy distribution of conversion electrons. . . . .	67
5.13	Photon reconstruction efficiency, without the <i>no track</i> cut, as a function of the photon's energy. . . . .	67
6.1	The invariant mass distribution of the $B^\pm \rightarrow \chi_c K^\pm$ candidates in the three data sub-samples. . . . .	71
6.2	Comparison of several kinematical quantities between the Run 1A and Run 1B data. . . . .	73
6.3	Comparison of several kinematical quantities between the Run 1B $_\alpha$ and Run 1B $_\beta$ data. . . . .	76

# List of Tables

1.1	Classification of the fermions within the Standard Model . . . .	2
1.2	Experimentally determined fermion masses . . . . .	3
1.3	Properties of the elementary interactions of the Standard Model	3
2.1	Comparison of $b$ quark production cross sections with respect to the total interaction cross section at various existing and proposed colliders. . . . .	9
3.1	The operating conditions of the Tevatron during the 1992-5 running period. . . . .	27
4.1	Summary of the decay reconstruction parameters for the total data sample. The values and errors quoted in this table are only the results of statistical fits to the data. They do not include systematic errors which are expected to be larger than the statistical ones. . . . .	50
4.2	Comparison of the masses determined with this analysis ( $M_{Exp}$ ) with the global average values ( $M_{Avg}$ ). . . . .	51

6.1 Comparison of the $\chi_c K^\pm$ mass fit results for the three data sub-samples. . . . .	72
---	----

# Chapter 1

## Introduction

The current theoretical construct which attempts to explain the behavior of subatomic particles is known as the Standard Model (SM). Proposed in the 1970's to explain experimental results, the SM has since made several successful predictions regarding particle properties and interactions thus establishing itself as the leading theory of subatomic particles. One such renowned prediction was the twenty year old postulate of the existence of a sixth quark [1], named the top quark. The existence of the top quark was finally proven in 1995 by two experiments at Fermilab<sup>1</sup>[2].

Shortcomings of the SM, however, are believed to lie in its description of physics at energy- and time-scales approaching the Planck limits. These considerations have prompted the proposition of various extensions and alternatives to the SM. No evidence supporting any of those alternatives, however, has been discovered. Thus the Standard Model currently remains the most fundamental description of particle properties and interactions.

Quantum field theory [3] classifies all particles into two classes: fermions and bosons. Fermions are objects with half-integer spin,  $\mathbf{S} = 1/2, 3/2, \text{etc.} \dots$ ,

---

<sup>1</sup>The CDF and D0 experiments discovered direct evidence of the top quark in  $p\bar{p}$  collisions at  $\sqrt{s} = 1.8 \text{ TeV}$  at the Fermi National Accelerator Laboratory, Batavia, Illinois (Fermilab).

while bosons have integer spin,  $\mathbf{S} = 0, 1, 2$ , etc. . . . This classification applies to composite systems such as mesons, hadrons, and atoms as well as fundamental particles. Within the framework of the SM the fundamental particles constituting matter are fermions, while bosons are responsible for mediating the forces between the fermions. Fermions, in turn, are divided into two categories: leptons and quarks, based upon whether or not the fermion interacts via the strong force. The fundamental particles of the SM consist of six leptons: electron ( $e$ ), muon ( $\mu$ ), tau ( $\tau$ ), and electron, muon, and tau flavored neutrinos ( $\nu_e, \nu_\mu, \nu_\tau$ ); and six quarks: up ( $u$ ), down ( $d$ ), charm ( $c$ ), strange ( $s$ ), top ( $t$ ), and bottom ( $b$ ). The different quark types are referred to as flavours. All these particles have anti-particles with identical mass but opposite charge. There are 12 bosons in the SM; 8 gluons ( $g$ ) which mediate the strong force, 3 vector bosons ( $W^+, W^-,$  and  $Z$ ) which mediate the weak force and a photon ( $\gamma$ ) which mediates the electromagnetic force.

Fermions, both leptons and quarks, are also categorized into three generations; fundamental interactions within the SM are postulated to be identical among the generations up to kinematic factors dependent on the fermion's mass. Tables 1.1 and 1.2 illustrate the SM classification of the fermions and list their properties. Table 1.3 lists the fundamental forces and their properties.

Fermion	Generations			Charge
	1	2	3	
Leptons	$e$	$\mu$	$\tau$	-1
	$\nu_e$	$\nu_\mu$	$\nu_\tau$	0
Quarks	$u$	$c$	$t$	+2/3
	$d$	$s$	$b$	-1/3

Table 1.1: Classification of the fermions within the Standard Model [4]. The entries represent both particles and anti-particles, where the charge of the anti-particles is the negative of the charge of their particle counterpart. Particle charges are in units of the absolute electron charge.

Leptons		Quarks	
Particle	Mass ( $\text{MeV}/c^2$ )	Particle	Mass ( $\text{MeV}/c^2$ )
$e$	0.511	$u$	2–8
$\nu_e$	$< 5.1 \times 10^{-6}$	$d$	5–15
$\mu$	105.7	$c$	1000–1600
$\nu_\mu$	$< 0.17$	$s$	100–300
$\tau$	$1777.1 \pm^{+0.4}_{-0.5}$	$t$	$(1.76 \pm 0.13) \times 10^5$
$\nu_\tau$	$< 24$	$b$	4100–4500

Table 1.2: Experimentally determined fermion masses [5, 2]. The masses of the neutrinos are 90% confidence level upper-limits. The mass range for each of the quarks is a result of the various theoretical methods used to extract the mass.

Force	Strong	Weak	Electromagnetic
Mediator Boson	Gluon	$W^\pm, Z$	Photon
Mediator Mass ( $\text{GeV}/c^2$ )	massless	80.33, 91.19	massless
Range (m)	$\infty$	$10^{-18}$	$\infty$
Relative Strength	25	0.8	1
Interacting Fermions	Quarks	Quarks & Leptons	Quarks & $e, \mu, \tau$

Table 1.3: Properties of the elementary interactions of the Standard Model [4].

The electromagnetic and weak interactions can both be described by a single Lagrangian known as the ‘Standard Model of Electroweak Interactions’ [6, 7, 8], while the strong force is described by Quantum Chromodynamics (QCD) [9]<sup>2</sup>. An important aspect of the forces is the conservation laws they obey. The electromagnetic and strong forces conserve flavour, therefore, a strongly or electromagnetically interacting quark (lepton) will retain its flavour. The weak force on the other hand does not conserve flavour; a weakly interacting *up*-type quark ( $u, c, t$ ) may be transformed into a *down*-type quark ( $d, s, b$ ). Similarly, weakly interacting charged leptons may be transformed into neutrinos, and the analogous interactions where a *down*-type quark (neutrino) interacts weakly will result in an *up*-type quark (charged lepton).

<sup>2</sup> Attempts at incorporating gravity into the SM at energy- and distance-scales of elementary particle interactions have been unsuccessful so far.

The quark flavours referred to so far are known as quark mass eigenstates; they are also strong and electromagnetic force eigenstates since these forces conserve quark flavour. If the quark mass eigenstates were also weak force eigenstates then the transitions from one flavour to another due to the weak force would remain within the same generation, i. e. the only allowed flavour transitions would be  $u \Leftrightarrow d, c \Leftrightarrow s, t \Leftrightarrow b$ . The quark mass eigenstates, however, are not eigenstates of the weak force; this means that transitions to quark flavours from different generations are allowed. Such transitions are described by the Cabibo-Kobayashi-Maskawa (CKM) matrix [10] which relates the quark mass eigenstates to the weak force eigenstates as shown in equation 1.1.

$$\begin{pmatrix} d' \\ s' \\ b' \end{pmatrix} = \begin{pmatrix} V_{ud} & V_{us} & V_{ub} \\ V_{cd} & V_{cs} & V_{cb} \\ V_{td} & V_{ts} & V_{tb} \end{pmatrix} \begin{pmatrix} d \\ s \\ b \end{pmatrix} \quad (1.1)$$

The weak force eigenstates, denoted by the *primed* quarks, are linear combinations of the mass eigenstates. The *up* type quark mass and weak eigenstates are taken to be equal (eqn 1.2):

$$\begin{pmatrix} u' \\ c' \\ t' \end{pmatrix} = \begin{pmatrix} u \\ c \\ t \end{pmatrix} \quad (1.2)$$

The numerical value of the CKM matrix [5] is

$$\begin{pmatrix} 0.9745 - 0.9757 & 0.219 - 0.224 & 0.002 - 0.005 \\ 0.218 - 0.224 & 0.9736 - 0.9750 & 0.036 - 0.046 \\ 0.004 - 0.014 & 0.034 - 0.046 & 0.9989 - 0.9993 \end{pmatrix}$$

where the range of values illustrates the uncertainty on each matrix element. The large diagonal elements of the CKM matrix indicate that quark transition within the same generation are favoured over transitions to different generations (off-diagonal elements).

The nature and strengths of the fundamental forces allow for bound states of fermions to exist. The lifetimes of such bound states (composite particles) are dependent on the forces binding the constituent particles as well as the other interactions available to them. Bound states of the electromagnetic force include positronium as well as atoms and molecules, while there are no known bound states of the weak force. The nature of the strong force requires that all particles associated with it, i. e. quarks and gluons, can only exist in bound states and never in isolation. This is the reason why quarks and gluons cannot be observed directly. The known bound states of the strong force are combinations of a quark and an anti-quark (mesons) as well as three quarks(anti-quarks) (baryons), collectively known as hadrons.

The study of hadrons containing a  $b$  quark, known as  $B$  mesons and baryons, is called  $B$  physics.  $B$  mesons and baryons are the heaviest bound states of the strong force for which extensive experimental information exists, thus they offer a unique system with which to test the SM and QCD predictions. The large mass of the  $b$  quark, for example, allows its treatment in a non-relativistic manner in models of  $B$  mesons [11], thus enabling theoretical calculations of  $B$  meson properties. Various models of  $B$  mesons, both within the SM framework as well as the various extensions and alternatives, predict different values for the branching ratios ( $\mathcal{B.R.}$ ) of the  $B$  mesons into charmonium ( $c\bar{c}$ ) final states [12]. Studies of exclusive branching ratios of  $B$  meson decays can, therefore, provide some evidence with which the validity of such models can be evaluated. In addition, studies of exclusive branching ratios of  $B$  mesons can provide information about the production cross sections of  $B$  mesons. This is particularly relevant information in light of the current  $B$  meson production cross section measurement by CDF which is higher than theoretical predictions by a factor of two [13].

This thesis investigates the ratio of branching ratios

$$\frac{\mathcal{B.R.}(B^\pm \rightarrow \chi_c K^\pm)}{\mathcal{B.R.}(B^\pm \rightarrow J/\psi K^\pm)} \quad (1.3)$$

at the Collider Detector at Fermilab (CDF) experiment using the following decay chains of the  $B^\pm$  mesons:

$$B^\pm \rightarrow \chi_c K^\pm$$

$\swarrow$   
 $J/\psi \gamma$

$\swarrow$   
 $\mu^+ \mu^-$

and

$$B^\pm \rightarrow J/\psi K^\pm$$

$\swarrow$   
 $\mu^+ \mu^-$

This thesis is organized as follows: Chapter 2 describes  $B$  physics in more detail, highlighting the ability of CDF to perform such studies. Chapter 3 describes the CDF detector in general and the detector components relevant to this analysis in detail. The analysis is then described in chapters 4 and 5 and is followed by a conclusion in chapter 6.

## Chapter 2

### *B* physics at CDF

The CDF detector is located at the Fermilab Tevatron storage ring. The Tevatron (Fig 2.1) is a 6.28 km circumference ring which collides proton anti-proton beams with a center-of-mass energy of  $\sqrt{s} = 1.8$  TeV and an instantaneous luminosity of  $\mathcal{L} = 2 \times 10^{31} \text{ cm}^{-2}\text{s}^{-1}$ .

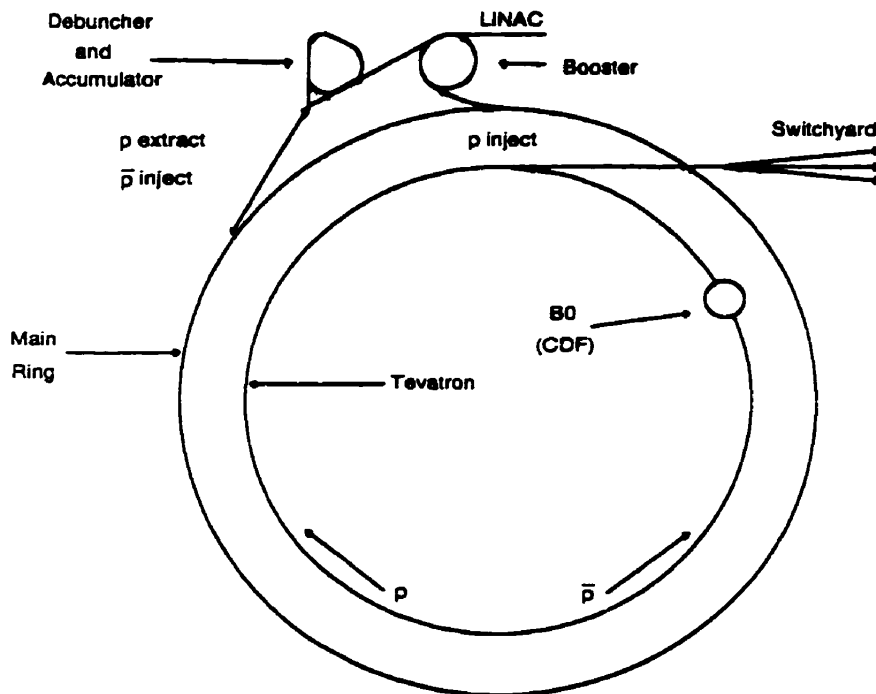


Figure 2.1: Illustration of the Tevatron main storage and acceleration rings.

Particle physics programs being pursued at CDF range from QCD, electroweak, and heavy flavor physics to searches for exotic phenomena. The heavy flavor program led to the discovery of the top quark in 1995 [2]. The large center-of-mass energy allows CDF to investigate high momentum transfer ( $Q^2$ ) phenomena which can test the SM as well as leading and next-to-leading order QCD approximations to a high degree of accuracy. The large  $W$  production cross section, ( $\sigma_W = 23$  nb [14]), translates into a large data sample of  $W$  decays and the world's most accurate measurement of the  $W$  mass. The large interaction cross section at CDF also translates into a large  $B$  meson production cross section:  $\sigma_B(P_T(B^+) > 6 \text{ GeV}/c, |\eta| < 1.0) = 2.5 \mu\text{b}$  [13]. Although CDF was not designed with the goal of studying  $B$  physics it became evident that such studies are indeed possible. Using a  $110 \text{ pb}^{-1}$  data sample collected from 1992-95, CDF has performed measurements of  $B$  meson masses [15], lifetimes [16] and branching ratios [17], among others. It is expected that with the higher luminosities and detector upgrade of the upcoming running period the  $B$  physics program at CDF will be able to compete with those of dedicated  $B$  physics experiments such as BaBar and Belle, possibly allowing a measurement of CP violation<sup>1</sup>.

The relatively large cross section for light quark and gluon production at a  $p\bar{p}$  collider such as the Tevatron is a disadvantage since such events constitute background for the  $B$  physics studies. Table 2.1 compares the  $b\bar{b}$  production cross sections,  $\sigma_{b\bar{b}}$ , and total interaction cross sections<sup>2</sup>,  $\sigma_{tot}$ , between the Tevatron and various existing and proposed  $p\bar{p}$  and  $e^+e^-$  colliders. In order to reduce the large background rate and obtain a data sample with a higher fraction of  $b$  quark and  $B$  meson decays, triggers are used to select and categorize events based on  $b$  quark and  $B$  meson decay signatures. Those signatures

<sup>1</sup>CP violation is the violation of the charge conjugation (C) and parity (P) symmetries and is expected to be measurable in the neutral  $B$  meson system.

<sup>2</sup>The total interaction cross section,  $\sigma_{tot}$ , is not well defined for  $p\bar{p}$  colliders and is usually taken to mean the total inelastic interaction cross section.

Collider	Beams	$\sqrt{s}$ (TeV)	$\sigma_{b\bar{b}}$ ( $\mu\text{b}$ )	$\sigma_{\text{tot}}/\sigma_{b\bar{b}}$
Tevatron	$p\bar{p}$	1.8	50	1000
S $\bar{p}p$ S	$p\bar{p}$	0.63	10	5000
LHC	$p\bar{p}$	14	200	500
CESR	$e^+e^-$	0.0095	$1.1 \times 10^{-3}$	4
LEP	$e^+e^-$	0.091	$5.0 \times 10^{-3}$	7
PEP II	$e^+e^-$	0.010	$1.0 \times 10^{-4}$	3

Table 2.1: Comparison of  $b$  quark production cross sections with respect to the total interaction cross section at various existing and proposed colliders.

are chosen based on the decay modes of interest of the  $B$  mesons, namely:  $B^\pm \rightarrow \chi_c K^\pm$  and  $B^\pm \rightarrow J/\psi K^\pm$ . For the remainder of this chapter mentions of a specific particle or decay process refer to the charge conjugate particle or process as well.

$B^-$  mesons consist of  $\bar{u}b$  quarks. Since the strong and electromagnetic forces conserve quark flavour, the only way  $B^-$  mesons can decay is through the weak force where the  $b$  quark emits a  $W^-$  and turns into a  $c$  or  $u$  quark<sup>3</sup> as shown in figure 2.2. The fraction of  $b \rightarrow c$  quark decays with respect to  $b \rightarrow u$

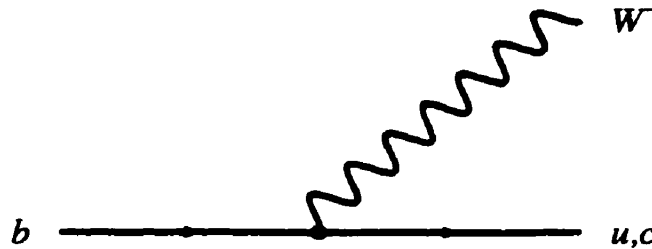


Figure 2.2: Feynman diagram of the  $b$  quark decay by the emission of a  $W^-$  boson.

quark decays is given by  $|V_{cb}/V_{ub}|^2 \sim 175$ . A model of heavy quark meson decays, the spectator model, describes  $B^-$  meson decay by assuming that the

<sup>3</sup>Although the  $b \rightarrow t$  transition is theoretically allowed and has a large CKM matrix element, it is kinematically forbidden in  $B$  meson decays due to energy conservation.

light quark ( $u$ ) is a spectator to the heavy quark ( $b$ ) decay and combines with its decay products to form a particular final state as shown in figure 2.3 for the  $B^\pm \rightarrow J/\psi K^\pm$  and  $B^- \rightarrow \chi_c K^-$  decays. If the  $c\bar{c}$  state, resulting from

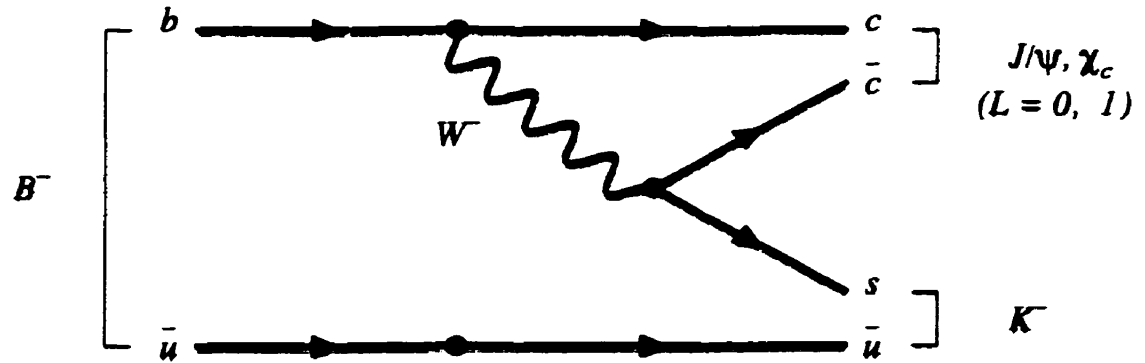
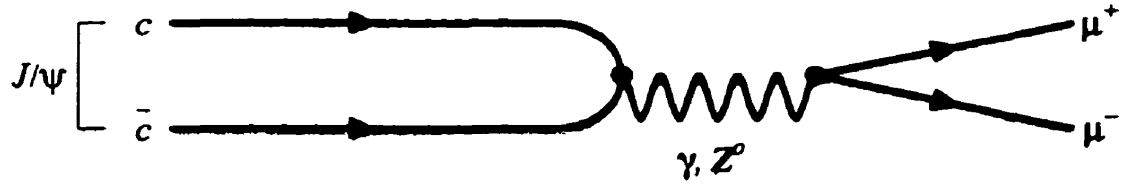
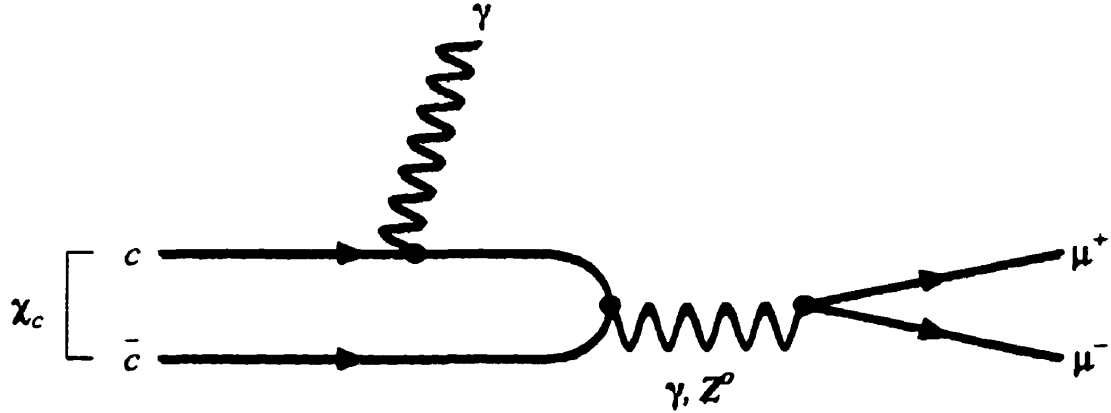


Figure 2.3: Feynman diagram of the  $B^-$  meson decays  $B^- \rightarrow J/\psi K^-$  and  $B^- \rightarrow \chi_c K^-$ .

the  $B^\pm$  decay, had a total angular momentum  $\mathbf{L} = 1$  instead of  $\mathbf{L} = 0$  then it would have been a  $\chi_c$  instead of a  $J/\psi$ . The name  $\chi_c$  refers to three distinct  $c\bar{c}$  states:  $\chi_{c0}$ ,  $\chi_{c1}$ , and  $\chi_{c2}$ . The three  $\chi_c$  states have slightly different masses, their defining characteristic, however, being the total angular momentum  $\mathbf{J} = 0, 1, 2$  respectively.

The  $K^-$  is a long lived particle<sup>4</sup> and can therefore leave a detectable track in CDF. The  $K^-$  cannot be triggered on, however, since there is not enough information available to distinguish it from the numerous other charged tracks, such as pions and electrons, present in the event in the time span available to the trigger. Muons, however, are readily identified by the trigger; therefore we use the two muons from the decays of the  $\chi_c$  and  $J/\psi$ :  $\chi_c \rightarrow J/\psi \gamma$ ;  $J/\psi \rightarrow \mu^+ \mu^-$  (Figs 2.4 and 2.5) as a signature of a  $B^\pm$  meson decay. This analysis used data collected by a trigger which required two muon candidates in the

<sup>4</sup>The lifetime of the  $K^-$  is  $\tau = 1.237 \times 10^{-8}$  s. Therefore the mean distance travelled by a relativistic  $K^-$  is  $\gamma c \tau = 3.709$  m.

Figure 2.4: Feynman diagram of the  $J/\psi$  meson decay into  $\mu^+\mu^-$ .Figure 2.5: Feynman diagram of the  $\chi_c$  meson decay into  $\mu^+\mu^-\gamma$ .

final state. Even though the branching ratios of the above mentioned decays  $\chi_c$ <sup>5</sup> and  $J/\psi$  are only 27.3% and 5.97% respectively, they are used as an event signature since the number of background events with a similar signature is relatively small. Therefore

$$\frac{\mathcal{B.R.}(\chi_c \rightarrow J/\psi \gamma) \cdot \mathcal{B.R.}(J/\psi \rightarrow \mu^+\mu^-)}{\mathcal{B.R.}(p\bar{p} \rightarrow \mu\mu + X)} \gg \frac{\mathcal{B.R.}(\chi_c \rightarrow X)}{\mathcal{B.R.}(p\bar{p} \rightarrow X)} \quad (2.1)$$

and the ratio of *B* physics events in the data sample passing the trigger is much larger than the fraction of the total *B* physics event rate to the total interaction rate.

<sup>5</sup>The branching ratio quoted for  $\chi_c$  is that of the  $\chi_{c1}$  since it is the largest branching ratio of the three  $\chi_c$  states for this particular decay mode.

# Chapter 3

## The CDF Detector

### 3.1 Introduction

The CDF detector is a magnetic spectrometer. Protons and anti-protons collide at the center of the detector and final state particles exit in all directions uniformly distributed in rapidity<sup>1</sup>. The CDF detector covers 98% of the full solid angle and is able to detect outgoing particles with a minimum angle of 2° with respect to the beam line.

The innermost detector component is the Silicon Vertex Detector (SVX) whose purpose is to measure displaced decay vertices with a very high precision. Outside the SVX is the Central Tracking Chamber (CTC). The CTC records the position and momentum of charged particles as they traverse it. Both the CTC and the SVX are immersed in a 1.4 T solenoidal magnetic field created by a coil just outside the CTC. Outside the solenoid coil are Central Preradiator Chambers (CPR) followed by the Central Calorimeters, muon detectors, and the return yoke for the magnetic field. The purpose of the CPR is to detect electrons from photons which have converted in the 0.8 radiation length thick ( $X_0$ ) solenoid.

---

<sup>1</sup>Rapidity,  $y$ , is given by  $y = \frac{1}{2} \ln\left(\frac{E+P_z}{E-P_z}\right)$  where  $P_z$  is the component of the momentum along the  $z$  axis.

In order to obtain the best possible coverage close to the beam line, components of the calorimeter and the muon detectors, called the Forward/Plug Calorimeters and Forward Muon Toroids, are placed up and down stream of the nominal collision point at the center of the detector. Up and down stream of the collision point are also a set of scintillator hodoscopes known as Beam Beam Counters (BBC), the main purpose of which is to measure the instantaneous luminosity being delivered by the Tevatron. Figure 3.1 is a schematic representation of one quadrant of the CDF detector.

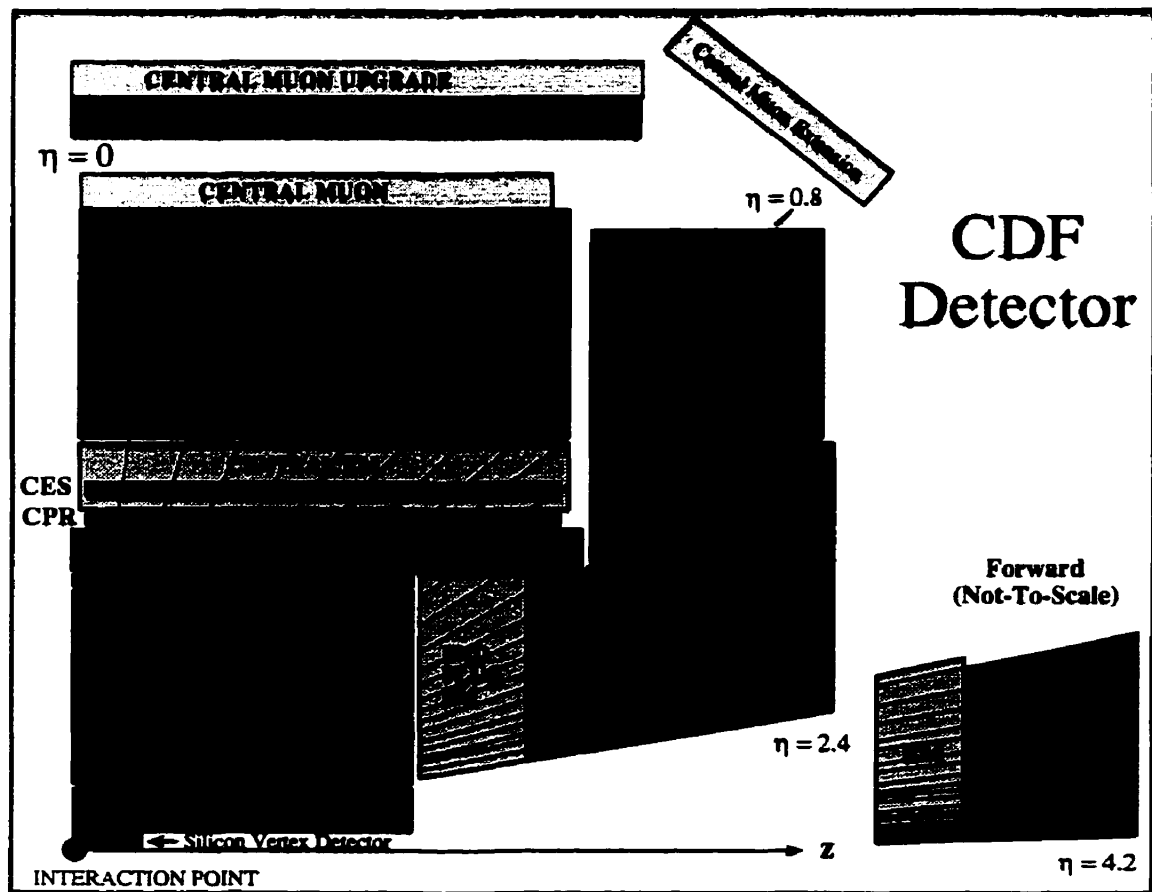


Figure 3.1: Schematic drawing of the CDF detector. The detector is symmetric about the interaction point in both the horizontal and vertical axis. The calorimeter is shown segmented in units of  $\eta = 0.1$ .

The CDF coordinate system is defined as follows. The  $z$ -axis lies along the beams, with positive  $z$  pointing along the proton beam direction. The  $y$ -axis

points vertically upward and the  $x$ -axis is such that the coordinate system is right handed and orthogonal. Due to the cylindrical symmetry of the detector a more convenient coordinate frame is defined by  $(r, \phi, \eta)$ , where  $r$  is the radial distance of a point from the  $z$  axis and  $\phi$  is its azimuthal angle, measured from the  $x$ -axis.  $\eta$  is a variable that provides information orthogonal to the  $r - \phi$  plane. It is called pseudo-rapidity and is given by  $\eta = -\ln(\tan(\theta/2))$  where  $\theta$  is the polar angle with respect to the  $z$ -axis. Pseudo-rapidity is derived from rapidity ( $y$ ) with the assumption of massless particles<sup>2</sup>, and at high energies  $\eta \approx y$ . The calorimeters are segmented in units of  $\eta$  since the final state particle density of a hadronic collision is almost constant as a function of  $\eta$ .

For energetic  $p\bar{p}$  collisions, such as the 1.8 TeV center-of-mass energy of the Tevatron, the collision is described by the scattering of quarks/gluons in the proton from those in the anti-proton. The scattering particles, however, carry an unknown fraction of the (anti)proton's momentum. This means that the net momentum along the  $z$ -axis,  $P_z$ , of the interacting particles is unknown, and may indeed be large.  $P_z$ , however, cannot be accurately measured since a significant fraction of the collision products escape through uninstrumented regions down the beam pipe. Consequently, conservation of  $P_z$  cannot be used to constrain the collision kinematics since the total  $P_z$  is unknown and unmeasurable. The transverse momentum,  $P_T = P_X^2 + P_Y^2 = |\vec{P}| \sin \theta$ , of the interacting particles, however, is always zero. Hence conservation of transverse momentum remains a valid means of constraining the collision kinematics. Consequently, information in the transverse plane, such as momentum and position, is very important for physical analyses and the CDF detector has been designed to minimize the measurement resolution of these quantities. Measurement resolutions in the  $z$  direction, however, are usually an order of magnitude larger. In situations where the center-of-mass momentum is unknown, such as  $p\bar{p}$  collisions, rapidity (pseudo-rapidity) is a useful kinematical

---

<sup>2</sup>Hence the name pseudo-rapidity.

variable due to its additive transformation properties under Lorentz boosts. Quantities which are measured in the detector frame of reference cannot be transformed into the center-of-mass frame of reference without knowledge of its boost with respect to the detector frame of reference. Since rapidities are additive under Lorentz boosts, the difference of rapidities and the shape of distributions as a function of rapidity will be independent of the center-of-mass boost.

The detector components that were significant for this analysis are the following:

- The Silicon Vertex Detector
- The Central Tracking Chamber
- The Calorimeters
- The Muon Chambers

and are described in more detail next.

### 3.1.1 The Silicon Vertex Detector

The SVX [18] is composed of four layers of single sided silicon substrates with a strip pitch of  $60 \mu\text{m}$  for the first three and  $55 \mu\text{m}$  for the fourth. The four layers are 50 cm long and are located at radii of  $r = 3.0, 4.3, 5.7,$  and  $7.9$  cm respectively where  $r$  refers to the radius of the center of the silicon wafer as shown in Fig 3.2. The SVX covers the region  $|\eta| < 1.9$  with the exception of a 2.15 cm gap at  $\eta = 0$ . Charged tracks passing through the SVX will create hits on a silicon layer with a 93% efficiency. This means that the efficiency for a track to have exactly three (four) hits in the SVX is 17% (75%). Therefore, the probability for a track having three or more hits is 92%.

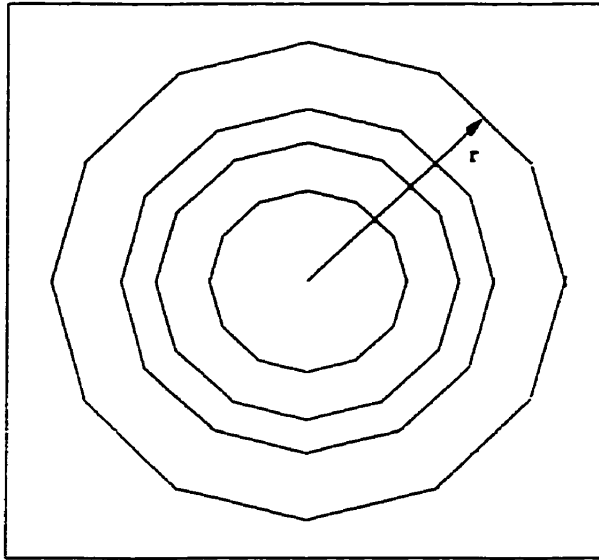


Figure 3.2: A cross-sectional view of the SVX.

For tracks with  $P_T = 3 \text{ GeV}/c$  the SVX produces an impact parameter measurement with a resolution of  $40 \mu\text{m}$ . For high  $P_T$  tracks the impact parameter resolution approaches  $10 \mu\text{m}$ . This allows the measurement of decay vertex positions with a resolution of  $50 \mu\text{m}$  in the  $r - \phi$  plane for vertices with three or more charged tracks originating from them.

The SVX is relevant in this analysis due to its ability to distinguish secondary decay vertices from the primary  $p\bar{p}$  collision vertex.  $B$  mesons typically have a lifetime  $\approx 1 \text{ ps}$  which means that the mean decay length of relativistic mesons is  $\approx 100 \mu\text{m}$ . For the fraction of  $B$  mesons with  $P_T > 6 \text{ GeV}/c$  and which do not immediately decay, the SVX is able to clearly distinguish between the meson's decay vertex and the  $p\bar{p}$  collision vertex. This allows the elimination of all short lived decays which constitute a large portion of the background to this analysis.

The SVX was replaced during the 1992-95 running period by another device, SVX', which had radiation hard electronics, but was otherwise identical in geometry and measurement resolution. When referring to the silicon ver-

text detector in a general manner the term SVX is used to mean either of the devices.

### 3.1.2 The Central Tracking Chamber

The Central Tracking Chamber [19] is the main detector component for measuring the position of charged particle tracks. Since the CTC is immersed in a magnetic field ( $B$ ) charged particles will move along a helical trajectory; the radius of curvature ( $R$ ) of which provides information about the particle's momentum:

$$P_T = 0.3 Z B R \quad (3.1)$$

Where  $P_T$  is measured in units of  $\text{GeV}/c$ ,  $B$  in Tesla,  $R$  in meters, and  $Z$  in units of the electron charge. This equation is derived from the Lorentz force law, with the numerical factor, due to converting  $Z$  from Coulombs to units of electron charge and  $P_T$  from  $\text{kg m/s}$  to  $\text{GeV}/c$ :

$$\frac{e}{c (10^9 \text{eV}/c^2)} = \frac{1.602^{-19}}{(3 \times 10^8)(10^9 \times 1.782 \times 10^{-36})} = 0.2995 \quad (3.2)$$

For  $B = 1.4 \text{ T}$  and  $Z = 1$  we have:

$$P_T = 0.42 R \quad (3.3)$$

The CTC's fiducial volume covers  $28 \text{ cm} < r < 138 \text{ cm}$  and  $-160 \text{ cm} < z < 160 \text{ cm}$ . Therefore, tracks originating from the nominal interaction point at  $z = 0$  with  $P_T > 0.3 \text{ GeV}/c$  and  $|\eta| < 1.0$  can traverse the entire CTC radially and thus are reconstructed with better accuracy than tracks that exit through the endcaps of the CTC ( $|\eta| > 1.0$ ) or those that curl on themselves within the CTC ( $P_T < 0.3 \text{ GeV}/c$ ). Within the CTC are 84 cylindrical concentric layers of sense wires grouped into 9 superlayers (Fig 3.3). Five of the superlayers are axial layers, having the sense wires parallel to the beam line, containing 12

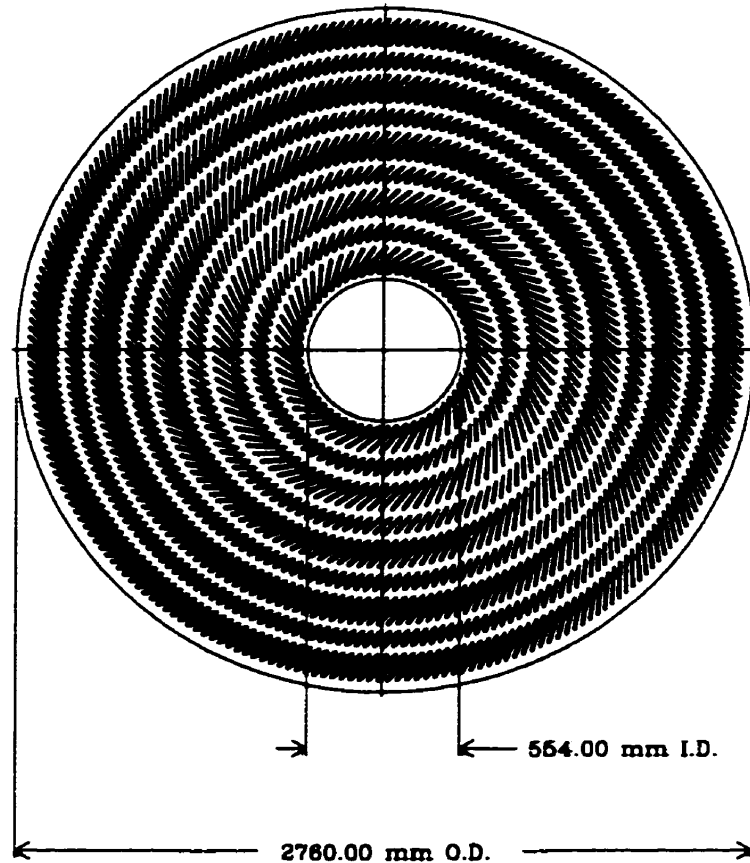


Figure 3.3: An end view of the CTC endplate showing the 9 tracking superlayers.

wire layers each. The remaining four superlayers are stereolayers with sense wire tilted by  $\pm 3^\circ$  with respect to the beam line and contain 6 wire layers each. The stereolayers provide a measurement of the  $z$  position of a track as well as its  $r - \phi$  position. Axial and stereo superlayers are arranged in an alternating manner. The gas used in the CTC is a 50%-50% mixture of argon-ethane bubbled through ethyl alcohol at  $-7.2^\circ \text{C}$ . This gas was chosen due to its performance parameters, such as its electron drift velocities, its response to impurities, and its aging effects, at the operating conditions of the CTC [20].

CTC sense wire hits are associated with tracks by an offline software al-

gorithm. The algorithm reconstructs track segments within each superlayer. Beginning at the outermost superlayer, the algorithm then attempts to match track segments across superlayers thus forming a whole track through the CTC. Track reconstruction is used to calibrate the CTC drift distance to drift time relationship function through an iterative procedure in which the drift distance to time relationship is updated based on the fitted drift distance of the tracks. The resulting position resolution for each sense wire hit is  $\approx 200 \mu\text{m}$  in  $r - \phi$ . With stereo information from adjacent layers a  $z$  resolution of 4 mm is obtained. For charged tracks with  $\theta_{\text{track}} = 90^\circ$  ( $\eta = 0$ ) a momentum resolution of  $\sigma_{P_T}/P_T^2 \leq 0.001 (\text{GeV}/c)^{-1}$  is achieved. The average momentum resolution for tracks throughout the CTC fiducial volume is  $\sigma_{P_T}/P_T^2 \leq 0.002 (\text{GeV}/c)^{-1}$ .

Since the path travelled by the charged particles through the CTC is a helix, each track found by the algorithm is represented by a helix via five parameters which fully and uniquely describe it. The five parameters used at CDF are  $(R, \phi, z_0, d_0, \cot \theta)$ .  $R$  is the radius of curvature of the track, from which the transverse momentum,  $P_T$ , of the track is obtained. The remaining four parameters, given with respect to the point-of-closest-approach to the  $z$ -axis, are the azimuthal angle of the track ( $\phi$ ), the  $z$  coordinate, the impact parameter ( $d_0$ ), and the cotangent of the polar angle of the track ( $\theta$ ) respectively.

Once tracks are constructed from the CTC information they are then extrapolated to determine where in the SVX the particles have passed. If hits are found in the SVX in the neighborhood of the extrapolated track positions then they are associated with that track and the track is re-fitted with the SVX information included. The central values of the track parameters are not changed significantly by including those few points, however, the uncertainty on those parameters improves considerably due to the good SVX resolution. Of relevance to this analysis is the resolution on  $d_0$ . Using solely CTC infor-

mation  $\sigma_{d0}$  has a mean of 200  $\mu\text{m}$  and a tail which extends to 400  $\mu\text{m}$ . If, however, the track parameters are fitted using both SVX and CTC information the mean of  $\sigma_{d0}$  becomes  $\approx 40\mu\text{m}$ .

### 3.1.3 The Central Calorimeters

The purpose of the CDF calorimeters is to measure the energy of the final state particles in the  $p\bar{p}$  interaction. Since neutral particles cannot be detected by either the SVX or the CTC the calorimeters are the only means of extracting any information about them. The calorimeters [21] are divided into four sections: the Central, End Wall, Plug, and Forward calorimeters. The four calorimeter sections cover the  $\eta$  regions:  $|\eta| < 1.1$ ,  $0.7 < |\eta| < 1.3$ ,  $1.1 < |\eta| < 2.4$ , and  $2.2 < |\eta| < 4.2$  respectively (Fig 3.1). Coverage in  $\phi$  is complete for all four sections. The calorimeters are segmented in  $\eta - \phi$  space into towers with dimensions  $0.1 \times 15^\circ$  ( $0.1 \times 5^\circ$ ) for the Central/End Wall (Plug/Forward) regions respectively. Figure 3.4 illustrates a central calorimeter wedge, which consists of ten towers grouped together to form a unit that is one unit in  $\eta$  and  $15^\circ$  in  $\phi$ . The wedges are symmetrically placed about  $\eta = 0$  ( $z = 0$ ) to form the central calorimeter.

Each calorimeter tower is divided into an electromagnetic and a hadronic component, with the hadronic component located radially behind the electromagnetic component. This is done in order to distinguish energy depositions (clusters) of photons and electrons from those of hadrons since hadrons have a larger penetration depth than photons/electrons. High energy photons and electrons interact predominantly by pair production and bremsstrahlung respectively. The distance that high energy photons/electrons penetrate through a material is characterized by its radiation length<sup>3</sup> ( $X_0$ ) which is inversely pro-

---

<sup>3</sup>The radiation length ( $X_0$ ) of a material is the distance a photon/electron traverses through the material before losing  $1/e$  of its energy.

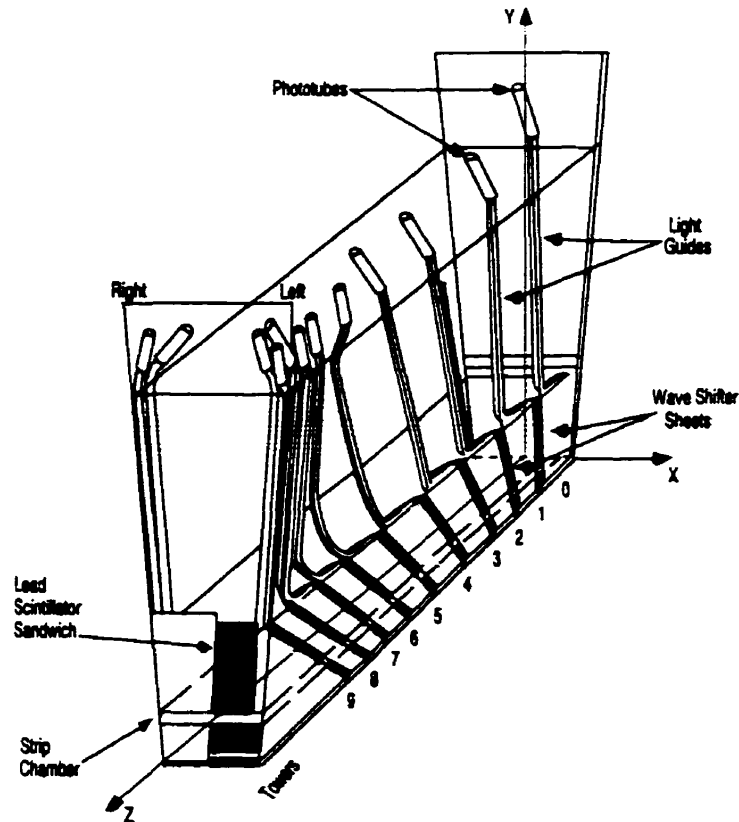


Figure 3.4: An illustration of the CEM towers in a calorimeter wedge. Also seen are the light guides that carry the output of the CEM to the phototubes.

portional to  $Z^2n$ , where  $n$  is the density of the material. Interaction of hadronic particles with calorimeter material includes elastic, inelastic, and quasi-elastic<sup>4</sup> scattering of the hadrons off nuclei. Since these interactions occur largely via the strong force the material with the largest cross section, and hence the smallest interaction lengths<sup>5</sup> ( $\lambda_I$ ) is the one with the highest atomic number,  $A$ . Consequently, the materials used for the hadronic and electromagnetic components of the calorimeter are different and are chosen based on their values of  $Z^2n$  and  $A$ .

<sup>4</sup>Quasi-elastic scattering is a process in which the interacting nucleus gets excited or broken up, but no new final state particles are created.

<sup>5</sup>Interaction length,  $\lambda_I$ , is analogous to the radiation length,  $X_0$ , where the incident particles are hadrons rather than photons/electrons.

The Central Electromagnetic Calorimeter (CEM) is made out of a lead-scintillator sandwich. Lead is used as the active material since it has a very high value of  $Z^2n$ . Wavelength shifters carry the light to a set of photomultiplier tubes located at the outer end of the calorimeter tower. The CEM is 32 cm thick, corresponding to  $18 X_0$  thus providing excellent hermeticity for electromagnetic showers and an energy resolution of

$$\frac{\sigma_E}{E} = \sqrt{\left(\frac{13\%}{\sqrt{E}}\right)^2 + (2\%)^2} \quad (3.4)$$

where  $E$  is the energy deposited in the CEM and measured in GeV. At a depth of  $5.9 X_0$ , corresponding to the depth at which an electromagnetic shower reaches its maximum lateral development, is a set of strip chambers (CES). The strip chambers are gas proportional chambers with a strip and wire read-out. The strip chamber is configured such that the wires are parallel to the  $z$ -axis while the strips are perpendicular to it and parallel to the face of the calorimeter tower, thus the CES is able to provide information in two dimensions. A local coordinate system is defined for the CES as follows. The CES  $z$ -axis is parallel to the global  $z$ -axis with the  $z_{CES} = 0$  point at  $\eta = 0$ , i.e. at the center of the calorimeter. The CES  $x$ -axis is parallel to the face of the CES and orthogonal to the CES  $z$ -axis. The CES measures the shape and position of electromagnetic energy clusters and serves the dual purpose of distinguishing photons/electrons from  $\pi^0$ s and determining the position of photons in the CDF detector. The distinction between photons/electrons and  $\pi^0$ s within the momentum range  $P_T < 100 \text{ GeV}/c$  is based on the fact that  $\pi^0$ s predominantly decay into two photons whose CES cluster shape differs significantly from that of a single photon if the electromagnetic clusters from two photons happen to partially overlap in the CES. If the overlap is large, however, such a distinction cannot be made. The latter function of the CES is very relevant to this analysis since it provides very accurate spatial information about the photon. A position resolution of the centroid of an electromagnetic shower of

$\pm 2$  mm, combined with a lever arm of 184 cm, the perpendicular distance from the beam line to the CES, gives a momentum direction resolution of  $0.062^\circ$ . This analysis only uses the Central calorimeters since the information provided by the CES is crucial to the reconstruction of the  $\chi_c$  decays. The End Wall, and Forward calorimeters do not have strip chambers.

The Central Hadronic Calorimeter (CHA) is made of iron-scintillator sandwich. It is  $4.7 \lambda_I$  thick and has an energy resolution of

$$\frac{\sigma_E}{E} = \sqrt{\left(\frac{75\%}{\sqrt{E}}\right)^2 + (3\%)^2} \quad (3.5)$$

where  $E$  is the energy deposited in the CHA and measured in GeV. Separate readouts for the CEM and CHA allow the measurement of the energy deposited in the electromagnetic and hadronic components of the calorimeter. Photons and electrons are expected to deposit most of their energy in the CEM and very little to none in the CHA; the presence of a track pointing towards the energy cluster distinguishes  $\gamma$ 's from  $e^\pm$ 's. Hadrons, such as  $\pi^\pm$ 's and  $K^\pm$ 's are expected to deposit most of their energy in the CHA, but with a non-negligible fraction in the CEM.

### 3.1.4 The Muon Chambers

The muon detectors [22] played an important role in this analysis since they were the detector components relevant to the trigger used to collect the data sample. Placed outside of the calorimeter, after more than  $5.5\lambda_I$  are several independent muon detectors which cover different regions of the solid angle. The muon detectors are:

- CMU Central Muon Detector
- CMP Central Muon Upgrade

- CMX Central Muon Extension
- FMU Forward Muon Toroids

The FMU was not used in this analysis and is not described. The CMU, CMP, and CMX together cover the region  $|\eta| < 1$  as shown in figure 3.5. Individually, the CMU and CMP cover the region  $|\eta| < 0.6$  with the CMP

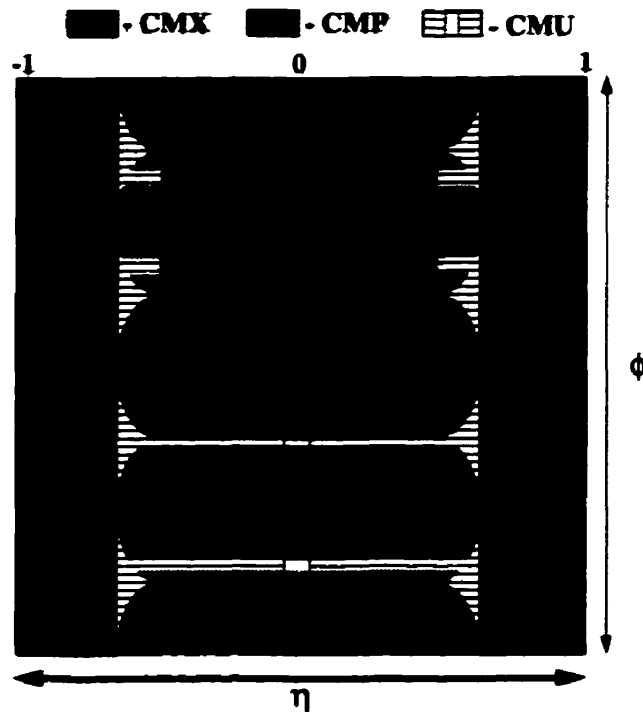


Figure 3.5: Schematic of the regions covered by each of the CMU, CMP, and CMX in  $\eta - \phi$  space. The circular features of the CMP coverage is simply the shape of a square in  $\eta - \phi$  space.

being placed outside of the CMU after an additional  $2.3\lambda_I$  of steel. The CMX covers the region  $0.6 < |\eta| < 1$ .

Muons are minimum ionizing particles as they pass through the calorimeter. Muons with transverse momentum less than  $1.4 \text{ GeV}/c$  are usually stopped

by the calorimeter; however, more energetic muons can penetrate through to the CMU and CMX. In order for muons to reach the CMP they must have  $P_T > 2.2 \text{ GeV}/c$ . Maximum detection efficiency, however, is only achieved for muons with  $P_T > 3.0 \text{ GeV}/c$ .

The CMU muon chambers consist of a number of single wire drift chambers (cells). The cells are  $63.5 \text{ mm}$  wide,  $26.8 \text{ mm}$  high, and  $2260 \text{ mm}$  long and are grouped into modules consisting of four layers of four cells each. Each calorimeter wedge contains three modules as shown in Fig 3.6. For two alternating lay-

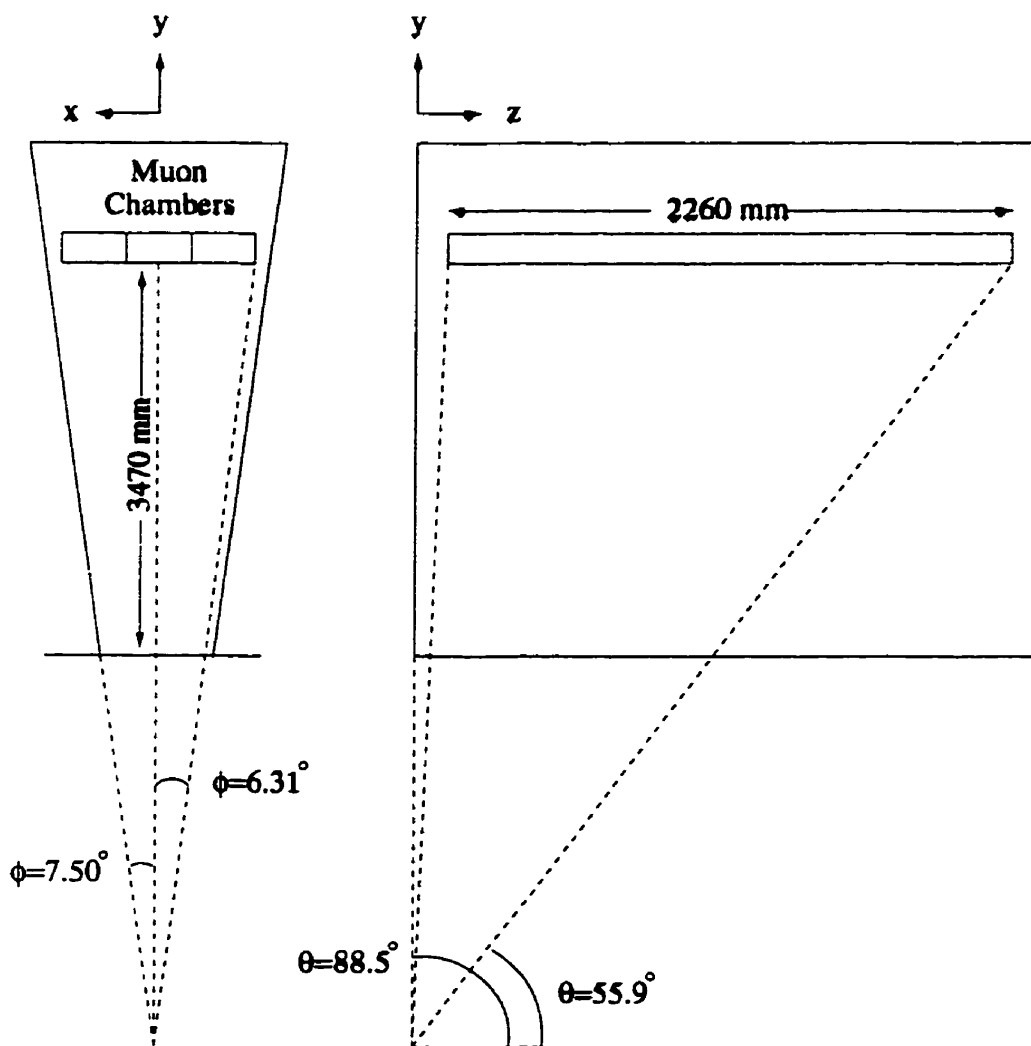


Figure 3.6: Schematic of the muon chamber wedges.

ers, the sense wires are placed at the center of the cell, along a radial line from the origin of the detector. For the other two layers the wires are placed along a line offset by 2 mm from the radial line as shown in Fig 3.7. This is done in

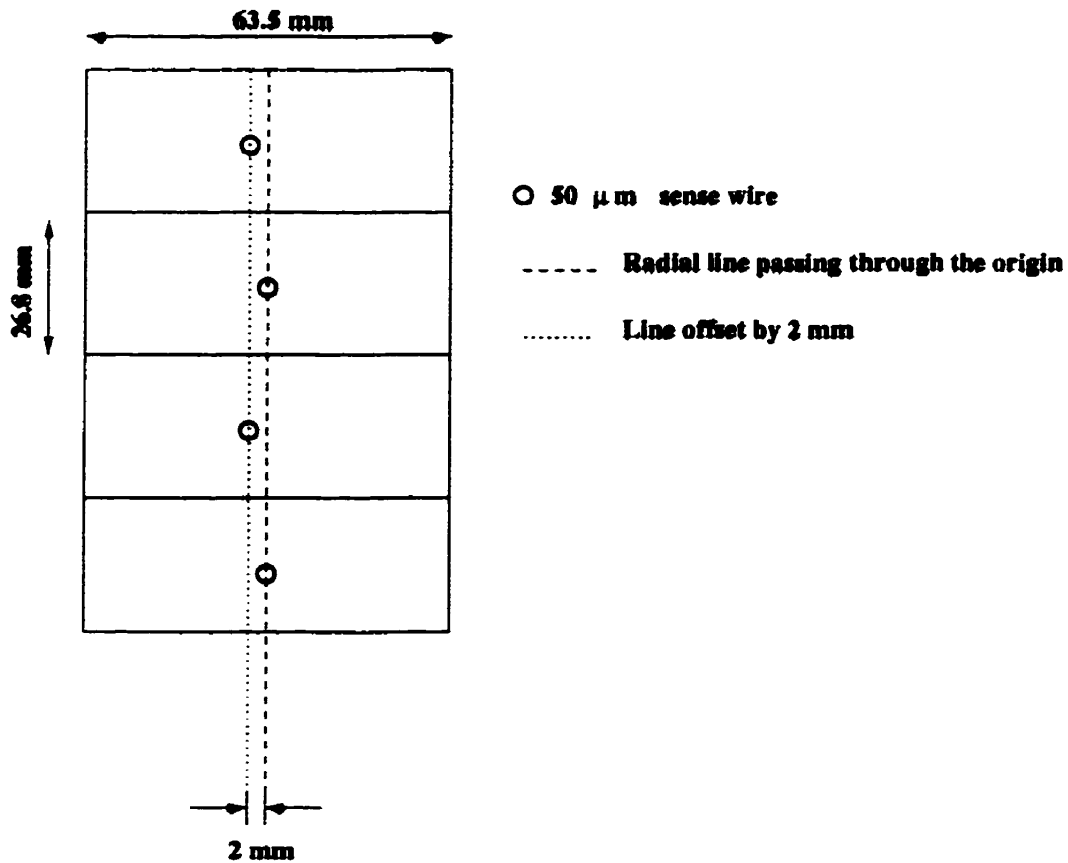


Figure 3.7: Illustration of the sense wire configuration in a CMU muon tower.

order to resolve the left-right ambiguity of a track passing through the tower (four radially consecutive muon drift chambers). The CMP (CMX) consists of single wire drift chambers with dimensions:  $150 \times 25 \times 6400$  (1800) mm. The CMP drift chambers form a box around the CDF detector while the CMX drift chambers lie on a conical surface whose axis coincides with the  $z$ -axis.

Within the CMU, track segments (stubs) are measured with a spatial resolution of  $250 \mu\text{m}$  in the  $r - \phi$  plane and  $1.2 \text{ mm}$  along the  $z$  axis. A more relevant quantity, however, is the amount of multiple scattering (multiple scattering resolution) a muon undergoes between entering the calorimeter and the muon detector. This is important since it governs how well a track reconstructed with the CTC can be extrapolated to match a stub in the CMU/CMP/CMX. If such an extrapolation is possible then the CTC track and muon stub are associated with each other and form a muon candidate. The multiple scattering resolutions for the CMU, CMP, and CMX are  $12 \text{ cm/P}$ ,  $15 \text{ cm/P}$ , and  $13 \text{ cm/P}$  respectively, where P is measured in  $\text{GeV}/c$  [23].

### 3.2 The CDF Trigger

The operating conditions of the Tevatron during the 1992-5 running period are described in Table 3.1. The inelastic interaction rate ( $W_{inel}$ ) is a dominant

Tevatron 1992-95	
Beam Types	$p\bar{p}$
Beam Energy	0.9 TeV
Bunches per Beam	6
$\Delta\tau_{\text{BunchCrossing}}$	$3.5 \mu\text{s}$
Luminosity ( $\mathcal{L}$ )	$2 \times 10^{31} \text{ cm}^{-2}\text{s}^{-1}$
Inelastic Cross Section ( $\sigma_{inel}$ )	50 mb
Inelastic Interaction rate ( $W_{inel}$ )	1 MHz

Table 3.1: The operating conditions of the Tevatron during the 1992-5 running period.

component of the total interaction rate at the CDF detector. Other contributions to the total interaction rate include elastic  $p\bar{p}$  scattering, beam-gas and beam-pipe collisions and cosmic rays. Since the data acquisition and storage capabilities of the experiment are limited not all the interactions detected by CDF (events) can be recorded. A trigger system [21] is used to select events

which are of interest to physical analysis at a rate consistent with the capabilities of the data acquisition and storage systems. Event selection is based on event signatures which distinguish the physical processes of interest from background events. The majority of event selection (or rejection) has to be made on a timescale smaller than the bunch crossing time of  $3.5 \mu\text{s}$  in order that events from the subsequent bunch crossings be considered.

CDF accomplishes this task by using a three level trigger to reduce the event rate from  $\sim 1 \text{ MHz}$  down to  $\sim 10 \text{ Hz}$  which is the rate at which events can be written to tape for storage. The Level 1 trigger is a hardware based trigger and is designed to reduce the  $\sim 1 \text{ MHz}$  event rate down to a  $\sim 1 \text{ kHz}$ . Using information from the fastest detector components, such as the calorimeters and the BBC's, the Level 1 trigger produces a decision regarding an event in less than  $3.5 \mu\text{s}$ . Levels 2 and 3 then reduce the accepted event rate to  $100 \text{ Hz}$  and  $10 \text{ Hz}$  respectively. The Level 2 trigger requires  $\sim 20 \mu\text{s}$  to produce a decision and has information from other, slower, detector components available. The  $20 \mu\text{s}$  decision time interval causes the subsequent 6 bunch crossing to pass unexamined; this illustrates the importance of reducing the the accepted event rate as much as possible with the Level 1 trigger. While an event is being considered by the Level 2 trigger the output of the entire detector is digitized and the event is prepared to be sent to the Level 3 trigger which is the most time intensive trigger. Unlike the Level 1 trigger which is completely hardware based, the Level 2 trigger uses a combination of hardware and software and Level 3 is totally software based. Using a software based Level 2 and Level 3 trigger allows for the modification of existing triggers or the implementation of new ones to look for different event signatures.

The data used in this analysis was collected with the *dimuon* trigger. At Level 1, the *dimuon* trigger requires hits (stubs) in at least two muon towers in either the CMU, CMP, or CMX with  $P_T > 1 \text{ GeV}/c$ . Online, the momentum

of a muon is determined by measuring the inclination of the track segment defined by the stub with respect to a radial line. At Level 2, CTC tracks are reconstructed in the  $r - \phi$  plane and extrapolated to the muon chambers. The Level 2 dimuon trigger requires that at least one of the muon stubs matches an extrapolated track within  $15^\circ$  in  $\phi$ . At Level 3, the CTC tracks are fully reconstructed, although with not as much precision as in the offline reconstruction. Both muon stubs are then required to match an extrapolated CTC track within  $4\sigma$  where  $\sigma$  is based on multiple scattering and measurement resolutions. The invariant mass of the two muon candidates ( $M_{\mu\mu}$ ) is also required to lie in the range:  $2.8 \text{ GeV}/c^2 < M_{\mu\mu} < 3.4 \text{ GeV}/c^2$ .

The 1992-95 running period was divided into two parts referred to as Run 1A and Run 1B. Integrated luminosities ( $\int \mathcal{L} dt$ ) of 19 and 90  $\text{pb}^{-1}$  were collected during Run 1A and Run 1B respectively.

### 3.3 Event Structure

Analyses are concerned with physical objects such as muons and photons rather than raw detector hits. Consequently, events passing the Level 3 trigger are processed by various offline software algorithms in order to transform all the detector electronic output into such physical objects. CDF data is stored in YBOS data bank structures [24]. Three generalized levels of YBOS banks exist for describing data from detector output to reconstructed physical objects:

1. Digital detector output.
2. Calibrated detector output.
3. Reconstructed physical objects.

Other banks exist which complete the information about the event, such as the run and event identification and the triggers which selected this event.

The first level of YBOS banks, commonly referred to as *detector* banks stores the digital output of the various detector components. Offline software algorithms then use these detector banks along with calibration functions and constants to create the second level of YBOS banks, *element* banks. The element banks contain a more physical description of the detector output such as the energy depositions in the calorimeter towers, however, they are still specific to a single detector component. *Segment* banks are the third level of YBOS banks. They are created by using information from several detector components to form a complete description of a physical object.

Of concern in this analysis is the creation of muon, photon, and charged track objects. Third level YBOS track banks describe the charged track ( $K^\pm$ ) candidates. These banks are called TRKS banks and are based solely on CTC information. If SVX as well as CTC information is used to determine the track parameters the results are stored in an SVXS bank. This analysis considers SVXS banks only if hits in at least three layers of the SVX were associated with the track. This is done in order to avoid SVX information due to random noise hits and subsequently underestimating the track measurement resolution.

CMUO banks, which provide information about the muon candidates, are created by extrapolating and matching a CTC track segment with a stub in the CMU/CMP/CMX. The CTC track segments are required to have a minimum transverse momentum of  $P_T > 1.5 \text{ GeV}/c$  in order to reduce misidentification of calorimeter punch-through<sup>6</sup> particles as muons.

---

<sup>6</sup>Since the calorimeters have a finite interaction length, some particles may leak through the end of a tower and cause hits in the muon detectors. These are referred to as punch-throughs.

CESS banks store information about the energies, shapes, and locations of energy clusters reconstructed in the CES along either the wire or strip views. This information is obtained by fitting the magnitude, shape, and position of the energy cluster in the CES to test beam data. The result of this fit is used to determine whether the energy cluster is due to a single photon/electron or to two photons from a  $\pi^0$  decay. The energy cluster is identified as a photon/electron if the  $\chi^2$  of the fit is small ( $\chi^2 \ll 20$ ). TOWE banks contain information about the magnitude of energy deposited in the various calorimeter towers. Unlike the CESS energy information which is derived from a fit to the shower shape in one sampling region, the TOWE energy information is that which is directly measured by the entire calorimeter tower. Photon candidates are reconstructed by identifying the calorimeter towers with more than 0.6 GeV of energy deposited in the electromagnetic component. For each such tower, the CESS banks are searched to determine whether there exist reconstructed energy clusters in the CES, in both the wire and strip views, within the boundaries of the tower. A single photon candidate is then associated with that TOWE/CESS combination with the energy of the photon taken from the TOWE bank and its position taken from the CESS banks. If more than one CES energy cluster falls within the boundaries of a tower, for a particular view, then the one with the highest energy is chosen.

# Chapter 4

## The $B^\pm$ Signal

The goal of this analysis is to measure the ratio of branching ratios

$$R = \frac{\mathcal{B.R.}(B^\pm \rightarrow \chi_c K^\pm)}{\mathcal{B.R.}(B^\pm \rightarrow J/\psi K^\pm)} \quad (4.1)$$

There are both theoretical and experimental reasons for measuring the branching ratios of the  $B^\pm$  meson relative to each other, rather than independently. Theoretically, the calculation of the ratio of branching ratios allows for the cancellation of certain terms which may be difficult to calculate or which are known with little accuracy. Such terms are related to the production mechanisms of the  $B^\pm$  mesons and include production cross-sections of the  $b$  quarks, their fragmentation into  $B^\pm$  mesons and the  $P_T$  spectra of the  $B^\pm$  mesons. These terms are independent of the decay mode of the  $B^\pm$  and hence will cancel when the ratio is taken. Experimentally, the branching ratio of a process can be determined, in principle, from the equation:

$$N_{tot}(B^\pm \rightarrow \chi_c K^\pm) = \int \mathcal{L} dt \cdot \sigma(B^\pm) \cdot \mathcal{B.R.}(B^\pm \rightarrow \chi_c K^\pm) \quad (4.2)$$

where  $N_{tot}$  is the total number of decays that actually occurred during the experiment. The absolute values of  $\int \mathcal{L} dt$ ,  $\sigma(B^\pm)$ , and  $N_{tot}$ , however, are not known with great accuracy. When the ratio of branching ratios is taken the

luminosity and cross-section terms will cancel; and  $R$  is given by:

$$R = \frac{\mathcal{B.R.}(B^\pm \rightarrow \chi_c K^\pm)}{\mathcal{B.R.}(B^\pm \rightarrow J/\psi K^\pm)} = \frac{N_{tot}(B^\pm \rightarrow \chi_c K^\pm)}{N_{tot}(B^\pm \rightarrow J/\psi K^\pm)} \quad (4.3)$$

In order to measure the value of  $R$  one must be able to reconstruct both decay modes from the CDF data to determine  $N_{tot}$  for each decay mode. The final state particles that are observed, however, are not the  $\chi_c$  or the  $J/\psi$  since their lifetimes are  $6.6 \times 10^{-20}$  s and  $7.5 \times 10^{-19}$  s [5] respectively. The decays through which the  $\chi_c$  and  $J/\psi$  are reconstructed are the following:

$$\chi_c \rightarrow J/\psi \gamma$$

and

$$J/\psi \rightarrow \mu^+ \mu^-$$

The  $K^\pm$ , being a long lived particle, is detected in the CTC. Therefore, the full decay chains which are considered are:

$$\begin{array}{l} B^\pm \rightarrow \chi_c K^\pm \\ \quad \quad \quad \swarrow \\ \quad \quad \quad J/\psi \gamma \\ \quad \quad \quad \quad \quad \swarrow \\ \quad \quad \quad \quad \quad \mu^+ \mu^- \end{array}$$

and

$$\begin{array}{l} B^\pm \rightarrow J/\psi K^\pm \\ \quad \quad \quad \swarrow \\ \quad \quad \quad \mu^+ \mu^- \end{array}$$

It should be noted that the three  $\chi_c$  states ( $\chi_{c0}, \chi_{c1}, \chi_{c2}$ ) have masses within 150 MeV/ $c^2$  of each other. The  $\chi_{c0}$  decays into a  $J/\psi$  and a photon with a branching ratio of  $(6.6 \pm 1.8) \times 10^{-1}\%$  compared to branching ratios of  $(27.3 \pm 1.6)\%$  and  $(13.5 \pm 1.1)\%$  for the  $\chi_{c1}$  and  $\chi_{c2}$  respectively. This means that the majority of reconstructed  $\chi_c$ 's will be  $\chi_{c1}$  and  $\chi_{c2}$  if production cross-sections of the three mesons are similar. These three  $\chi_c$  states have masses [5]

of

$$M_{\chi_{c0}} = 3.415 \text{ GeV}/c^2 \quad (4.4)$$

$$M_{\chi_{c1}} = 3.510 \text{ GeV}/c^2 \quad (4.5)$$

$$M_{\chi_{c2}} = 3.555 \text{ GeV}/c^2 \quad (4.6)$$

The mass difference,  $M_{\chi_{c2}} - M_{\chi_{c1}}$ , of  $45 \text{ MeV}/c^2$  is smaller than the mass resolution of the individual states with the CDF detector, hence the two mass states ( $\chi_{c1}$  and  $\chi_{c2}$ ) cannot be distinguished. The mass difference,  $M_{\chi_{c1}} - M_{\chi_{c0}}$ , of  $95 \text{ MeV}/c^2$  is barely larger than the mass resolution of the individual states, therefore, the two  $\chi_c$  states cannot be distinguished. Throughout this analysis the term  $\chi_c$  will refer to all three  $\chi_c$  states. However, the value of branching ratio  $\mathcal{B.R.}(\chi_c \rightarrow J/\psi \gamma)$  and mass used will only be those of the  $\chi_{c1}$ <sup>1</sup>.

Since this analysis only uses a particular final state of the  $\chi_c$  and  $J/\psi$  to reconstruct the  $B^\pm$  meson decay it is important to know the branching ratios of the  $\chi_c$  and  $J/\psi$  into that final state in order to correctly scale the number of reconstructed  $B^\pm$  meson decays. The branching ratio of the  $\chi_c$  into a photon and a  $J/\psi$  is

$$\mathcal{B.R.}(\chi_c \rightarrow J/\psi \gamma) = (27.3 \pm 1.6)\% \quad (4.7)$$

while the branching ratio of the  $J/\psi$  into two muons is

$$\mathcal{B.R.}(J/\psi \rightarrow \mu^+ \mu^-) = (5.97 \pm 0.25)\% \quad (4.8)$$

This means that only a fraction of the total  $B^\pm \rightarrow \chi_c K^\pm$  decays, given by

$$\mathcal{B.R.}(\chi_c \rightarrow J/\psi \gamma) \mathcal{B.R.}(J/\psi \rightarrow \mu^+ \mu^-) = 1.63\% \quad (4.9)$$

can be reconstructed via the decay chain used in this analysis. Similarly only 5.97% of the  $B^\pm \rightarrow J/\psi K^\pm$  decay can be reconstructed. The disadvantages of using such an infrequent decay chain are offset by the advantages of using the

<sup>1</sup>The  $\chi_{c1}$  was chosen since only the  $B^\pm \rightarrow \chi_{c1} K^\pm$  decay has been observed so far.

dimuon data sample which contains little non-muonic background and has a high trigger efficiency. In addition, reconstructing the  $B$  meson decay through an exclusive decay mode allows for good  $B^\pm$  mass resolution.

## 4.1 Reconstruction Strategy

### 4.1.1 Calculation of Invariant Masses

Invariant masses are calculated using the 3-momenta of decay product candidates and their corresponding mass assumption as shown in equations 4.10–4.13

$$M_{inv} = \sqrt{E_{tot}^2 - P_{tot}^2} \quad (4.10)$$

$$\vec{P}_{tot} = \Sigma_i \vec{P}_i \quad (4.11)$$

$$E_{tot} = \Sigma_i E_i \quad (4.12)$$

$$E_i = \sqrt{P_i^2 + M_i^2} \quad (4.13)$$

where  $M_{inv}$ ,  $E_{tot}$ , and  $\vec{P}_{tot}$  refer to the reconstructed particle, and  $M_i$ ,  $E_i$ , and  $\vec{P}_i$  refer to the decay products. Since the momenta of the final state particles have a non-zero measurement resolution the following techniques are used in order to improve the reconstructed particle mass resolution and to suppress background events:

1. Vertex constraint
2. Mass constraint
3. Pointing constraint

Vertex constraints require that the charged tracks being considered be consistent with originating from the same point in space (vertex) by varying the

track parameters to satisfy the vertex hypothesis. The vertex constraint is useful in suppressing background due to track combinations in which the tracks do not all originate from the same decay vertex and hence are not the decay products of a particular particle. The mass constraint fixes the invariant mass of the particles to a specified value and is useful in suppressing background in which the final state particles do not originate from the hypothesized particle decay. The pointing constraint requires that the sum of the momenta of the particles be parallel to the displacement vector between two specified points, namely the creation and decay vertices of a reconstructed particle. This constraint is useful for suppressing background events due to incorrect charged track combinations since the total momentum of a random track combination is uncorrelated with the displacement vector between the primary collision vertex and the possible point of intersection of the tracks.

All the constraints are applied in the form of a fit which adjusts the track parameters of the particles such that they satisfy the required constraints. For the cases in which the fit is successful a  $\chi^2$  is calculated based on the measurement errors of the track parameters and the amount by which they were adjusted. The probability that the particles in question satisfy the constraints is then calculated from the  $\chi^2$  and the number of degrees of freedom used in the fit.

### 4.1.2 Reconstruction of the Decay Chains

Since the muons, from the  $J/\psi$  decay, are common to both  $B$  decays we begin by searching for muons in each event and reconstructing the  $J/\psi$ 's. We consider all pairs of oppositely charged muons in the event as  $J/\psi$  candidates to be used in subsequent steps of the reconstruction.

For the  $B^\pm \rightarrow J/\psi K^\pm$  reconstruction we combine all the  $J/\psi$  candi-

dates with all charged tracks that are not associated with the  $J/\psi$  candidate. A vertex constraint is applied to the three charged tracks and the two muon candidates are mass constrained to the  $J/\psi$  world average mass of  $M_{J/\psi} = 3.0969 \text{ GeV}/c$ . Also, a pointing constraint is applied in which the  $p\bar{p}$  collision point and the vertex returned by the vertex constraint are used as the displacement vector's end points. In the surviving events a few such  $B^\pm \rightarrow J/\psi K^\pm$  candidates exist. Most of them, however, are still due to random combinations of charged tracks. In order to further reduce this type of background we accept the  $B$  meson candidate with the highest probability of satisfying the three constraint hypothesis. Such an approach is also physically motivated since  $B$  mesons are typically created in pairs in a  $p\bar{p}$  collision and the probability that both mesons decay into  $J/\psi K^\pm$  in the abovementioned manner is<sup>2</sup>  $(6.09 \cdot 10^{-5})^2 = 3.7 \cdot 10^{-9}$ .

The  $B^\pm \rightarrow \chi_c K^\pm$  reconstruction is similar to that of the  $B^\pm \rightarrow J/\psi K^\pm$ . After the  $J/\psi$  candidates have been identified they are each combined with photon candidates in order to construct  $\chi_c$  candidates. The momentum of the photon is taken to lie along the line connecting the  $J/\psi$  vertex and the centroid of the electromagnetic energy cluster. Once the  $\chi_c$  candidates are reconstructed they are then combined with all the  $K^\pm$  candidates in order to reconstruct the  $B^\pm$  meson. Just as in the  $B^\pm \rightarrow J/\psi K^\pm$  reconstruction the two muons are mass constrained to the  $J/\psi$  mass and the pointing and vertex constraints are applied. In addition, however, the energy of the photon is adjusted such that the invariant mass of the  $\chi_c$  candidate is equal to the  $\chi_{c1}$  world average mass of  $3.51053 \text{ GeV}/c^2$  ( $\chi_c$  mass constraint). Again, only one  $B^\pm \rightarrow \chi_c K^\pm$  candidate is accepted per event. However, in this case the majority of multiple  $B$  meson candidates in an event is due to multiple photon candidates in the reconstruction of the  $\chi_c$  rather than multiple  $K^\pm$  candidates.

---

<sup>2</sup>This number is arrived at by multiplying the branching ratios  $\mathcal{B.R.}(J/\psi \rightarrow \mu^+\mu^-)$  with the branching ratio  $\mathcal{B.R.}(B \rightarrow J/\psi K) = 1.02 \times 10^{-3}$  [5].

The chosen  $B$  meson candidate must have the highest probability of satisfying the vertex, mass, and pointing constraints. If several such candidates exist, each containing the same charged tracks but different photon candidates, then the one with the highest probability of satisfying the  $\chi_c$  mass constraint is chosen.

## 4.2 Selection Criteria

The data sample used in this analysis was taken by the dimuon trigger. This data sample, however, is dominated by events in which the two triggering muons did not originate from the decay of a  $B$  meson. Consequently, cuts have to be applied to the various physical objects in order to enhance the fraction of events containing a  $B$  meson which decayed as described above. These cuts were also designed to improve the identification efficiency of the various decay products and to minimize the resolution of their measured kinematical quantities. This section introduces and describes these cuts.

The physical motivation behind those cuts stems from the following arguments: Energy and transverse momentum spectra of  $p\bar{p}$  collision products are steeply falling. The large mass of the  $B$  meson ( $M_{B^\pm} = 5.2787 \text{ GeV}/c^2$ ), however, combined with the transverse momenta of the meson itself means that the small mass decay products, such as the muons, will have some significant boost in the transverse plane. Consequently, the  $P_T$  spectra of the  $B$  meson decay products will be less steeply falling than the average  $P_T$  spectrum, and a minimum muon  $P_T$  cut, for example, will produce a data sample with a larger fraction of events containing a  $B$  meson than the original data sample.

The efficiency of correctly identifying muon and photons candidates improves with increasing muon  $P_T$  and photon energy. A minimum  $E_\gamma$  cut is very important in this analysis since the number of fake photon candidates

from calorimeter noise decreases dramatically with an increasing  $E_\gamma$  cut.

### 4.2.1 Muon Selection

Muons reconstructed in the CMU, CMP, and CMX were used in this analysis if they satisfied the following cuts:

$$\chi_x^2 < 9.0 \quad (4.14)$$

$$\chi_z^2 < 12.0 \quad (4.15)$$

$\chi_x^2$  and  $\chi_z^2$  are the  $\chi^2$  on the extrapolation of the CTC track to the muon chamber stub in the  $x$  and  $z$  directions of the wedge coordinate frame respectively. The  $\chi^2$  distribution are shown in figures 4.1 and 4.2 with their respective cuts.

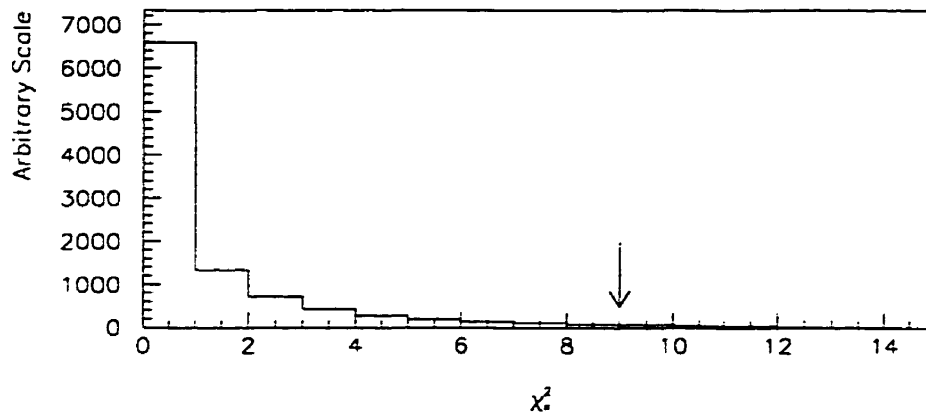


Figure 4.1: The  $\chi_x^2$  distribution of the muon candidates in the Run 1A data. The  $\chi^2$  distribution of the Run 1B data is similar to this. The arrow denoted the value of the  $\chi_x^2$  cut.

Figure 4.3 shows the momentum spectrum of muons passing the above cuts for the total dimuon data sample.

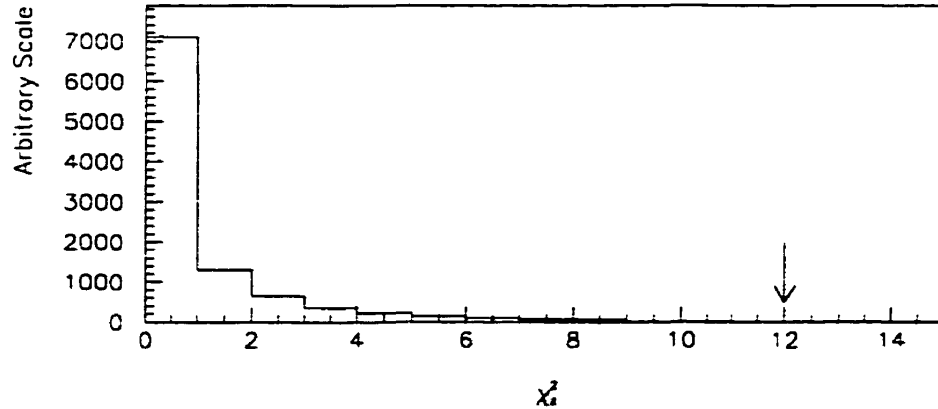


Figure 4.2: The  $\chi^2$  distribution of the muon candidates in the Run 1A data. The  $\chi^2$  distribution of the Run 1B data is similar to this. The arrow denoted the value of the  $\chi^2$  cut.

#### 4.2.2 $J/\psi$ Reconstruction

All oppositely charged muon candidates satisfying the vertex constraint were combined in pairs to form  $J/\psi$  candidates. To improve the  $J/\psi$  mass resolution and to reduce background combinations the following cuts were imposed :

- Smaller  $P_T$  of the two muons  $> 1.8 \text{ GeV}/c$
- Larger  $P_T$  of the two muons  $> 2.5 \text{ GeV}/c$
- $P_T(\mu^+\mu^-) > 4.0 \text{ GeV}/c$

The effectiveness of these cuts can be seen by comparing figure 4.3 with figures 5.5 and 5.6. Figure 4.4 shows the invariant mass distribution of the  $J/\psi$  candidates for the total data sample as well as for the individual Run 1A and Run 1B samples. For this plot all the  $J/\psi$  candidates in an event were included.

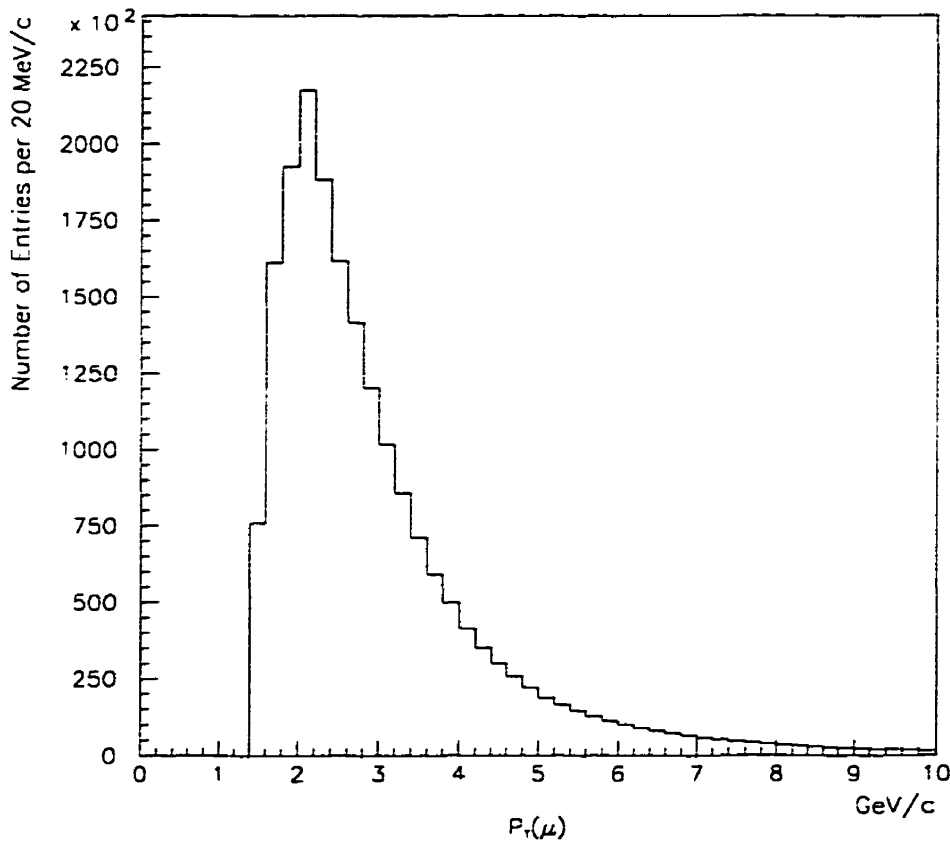


Figure 4.3: The  $P_T$  spectrum of the muons in the total data sample.

The  $\mu^+\mu^-$  invariant mass distribution was fitted to a sum of a Gaussian, which described the  $J/\psi$  mass peak, and a first order polynomial, which described the background. The fitted width of the Gaussian was  $\sigma_{M_{J/\psi}} = 0.021 \text{ GeV}/c^2$ , thus the  $J/\psi$  signal region, used for the subsequent steps in the  $B$  reconstruction, is

$$3.04 < M_{J/\psi} < 3.16 \text{ GeV}/c^2 \quad (4.16)$$

corresponding to  $3\sigma$  about the peak.

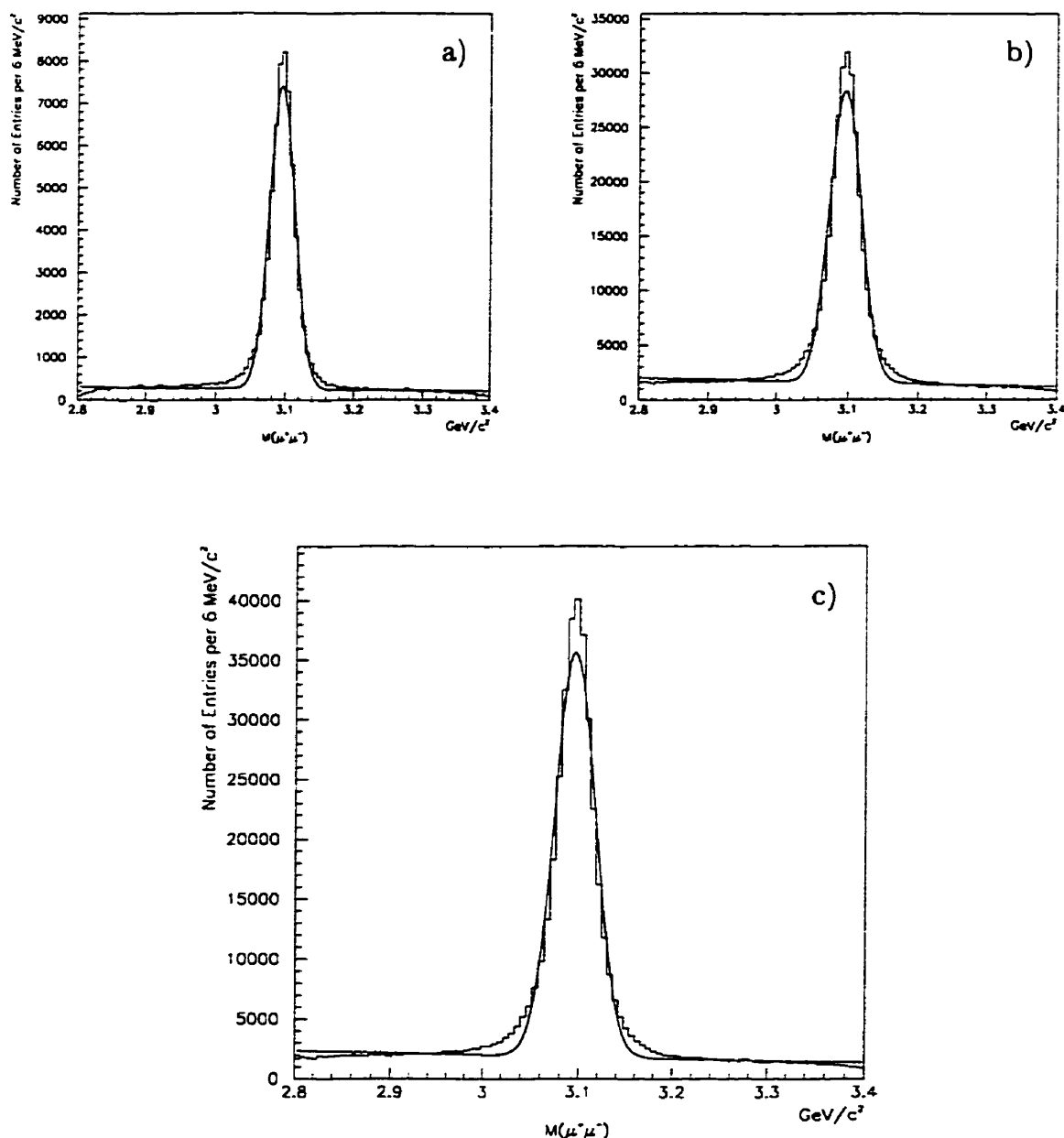


Figure 4.4: The invariant mass distribution of the  $J/\psi$  candidates. Plot a) shows the  $\mu^+\mu^-$  mass distribution for the Run 1A sample, while b) and c) show the  $\mu^+\mu^-$  mass distribution for the Run 1B and total samples respectively.

### 4.2.3 $K^\pm$ Selection

Since CDF does not have the ability to distinguish  $K^\pm$  tracks from the other charged tracks in an event for the momentum range relevant to this analysis, all

charged tracks were used as  $K^\pm$  candidates. A  $P_T$  cut of  $P_T(K^\pm) > 2 \text{ GeV}/c$  was applied for  $K^\pm$  candidates if the track was reconstructed only with CTC information (CTC track). If the track was constructed with SVX information as well (SVX track) then the  $P_T$  cut was relaxed to  $P_T(K^\pm) > 1.25 \text{ GeV}/c$ .

#### 4.2.4 $B^\pm \rightarrow J/\psi K^\pm$ Reconstruction

To further enhance the fraction of  $B$  mesons in the remaining events the following cuts were made on kinematical quantities of the reconstructed  $B$  candidates:

- $P_T(J/\psi K^\pm) > 6.0 \text{ GeV}/c$  if all three tracks were SVX tracks.
- $P_T(J/\psi K^\pm) > 8.0 \text{ GeV}/c$  if at least one track was not an SVX track.
- Probability of the tracks satisfying the combined vertex, mass, and pointing constraints  $> 0.5\%$ .
- Displacement of the  $B^\pm$  meson decay vertex in the transverse plane ( $L_{XY}$ )  $> 0.01 \text{ cm}$ .
- Isolation of the  $J/\psi K^\pm$  meson ( $\text{Isol}(J/\psi K^\pm)$ )  $> 0.55$ .
- Containment radius of the  $J/\psi K^\pm$  meson decay products ( $\text{Cont}(J/\psi K^\pm)$ )  $< 1.0$ .

$L_{XY}$  is the projection of the  $B^\pm$  meson displacement vector ( $\vec{D}$ ), in the  $r - \phi$  plane, onto its transverse momentum vector; where the displacement vector  $\vec{D}$  is defined by the primary ( $p\bar{p}$ ) collision vertex and the  $B^\pm$  decay vertex.

$$L_{XY} = \frac{\vec{D} \cdot \vec{P}_T}{|\vec{P}_T|} \quad (4.17)$$

$\text{Isol}(J/\psi K^\pm)$  is the fraction of transverse momentum carried by the  $J/\psi K^\pm$  in a cone of radius  $R = \sqrt{\eta^2 + \phi^2} = 1.0$ , centered around its momentum vector.

$$\text{Isol}(J/\psi K^\pm) = \frac{P_T(J/\psi K^\pm)}{P_T(J/\psi K^\pm) + \sum_i P_T^i} \quad (4.18)$$

The sum ranges over all tracks  $i$  within the cone, with  $P_T^i > 0.250 \text{ GeV}/c$ , that are not the  $B$  decay products.  $\text{Cont}(J/\psi K^\pm)$  is the radius of a cone in  $\eta - \phi$  space, centered around the  $J/\psi K^\pm$  meson momentum vector, which exactly contains all the decay products.

Figure 4.5 shows the invariant mass distributions of the  $B^\pm \rightarrow J/\psi K^\pm$  candidates for the Run 1A and Run 1B data as well as for the entire data sample. Figure 4.6 show the momentum distribution of the  $B^\pm \rightarrow J/\psi K^\pm$  candidates for the entire data sample.

### 4.2.5 $\gamma$ Selection

All energy clusters deposited in a single calorimeter tower, with corresponding strip and wire clusters in the CES and passing the following cuts are considered photon candidates:

- The wedge coordinates of the energy cluster satisfy:  $|x_{\text{wedge}}| < 20 \text{ cm}$ ,  $|z_{\text{wedge}}| > 10 \text{ cm}$  (fiducial volume cut)
- No CTC track extrapolates to the calorimeter tower containing the energy deposition.
- $E_\gamma > 1.0 \text{ GeV}$ .

The cut on the wedge coordinates of the energy clusters was made to ensure that the energy deposition was sufficiently far away from calorimeter tower borders where the calorimeter response is less understood.

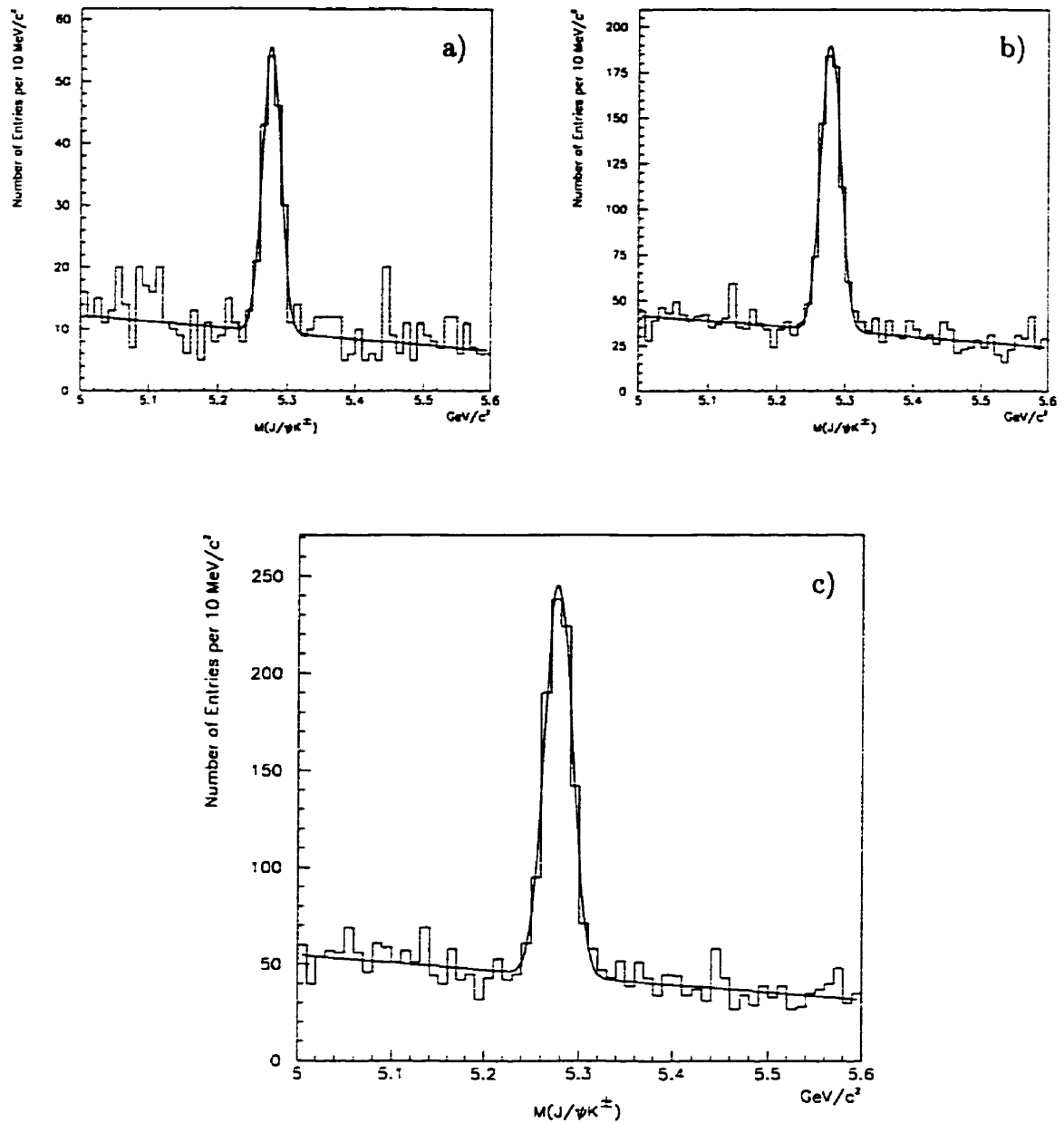


Figure 4.5: The  $J/\psi K^\pm$  invariant mass distribution. Plot a) shows the  $J/\psi K^\pm$  mass distribution for the Run 1A sample, while the b) and c) show the  $J/\psi K^\pm$  mass distribution for the Run 1B and total samples respectively.

#### 4.2.6 $\chi_c$ Reconstruction

$\chi_c$  candidates were formed by combining all the  $J/\psi$  candidates in an event with all the photon candidates. Figure 4.7 shows the  $\chi_c$  mass spectrum. What

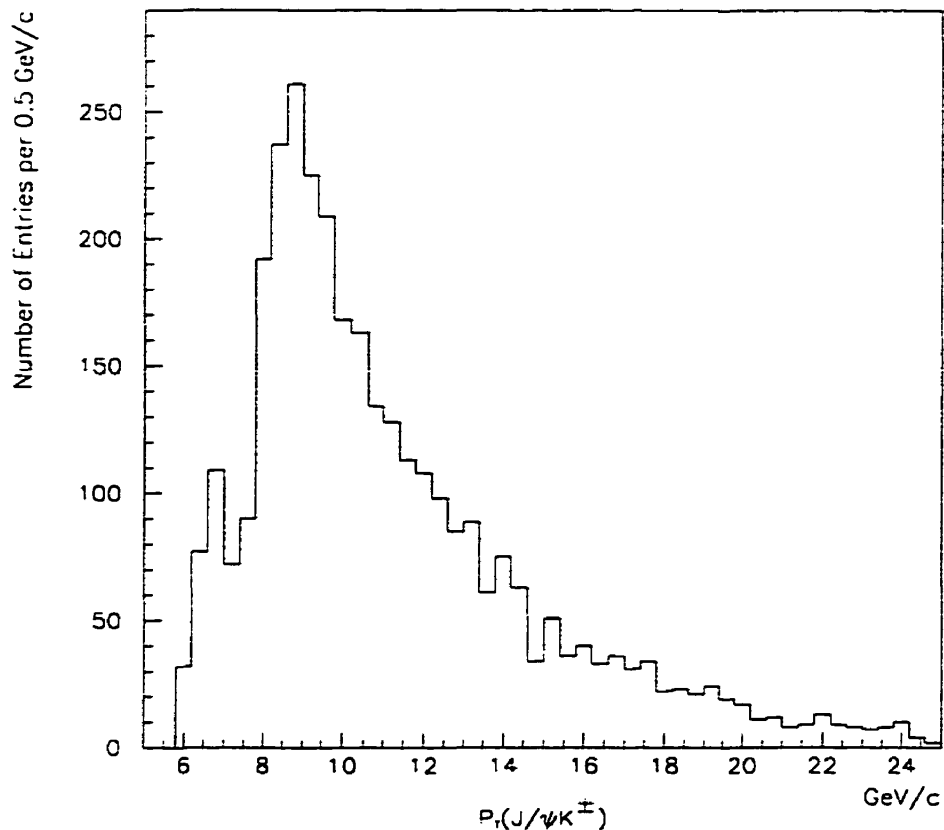


Figure 4.6: The  $P_T(J/\psi K^\pm)$  distribution for the entire data sample.

is actually plotted in figure 4.7 is the mass difference between a  $\chi_c$  candidate and the  $J/\psi$  from which it was reconstructed. This is done with the goal of decreasing the effects of systematic error associated with the charged tracks, and hence both the  $\chi_c$  and the  $J/\psi$ . Therefore, a better  $\chi_c$  mass resolution is obtained than would have been obtained otherwise. All  $\chi_c$  candidates found in an event are included in the mass spectrum.

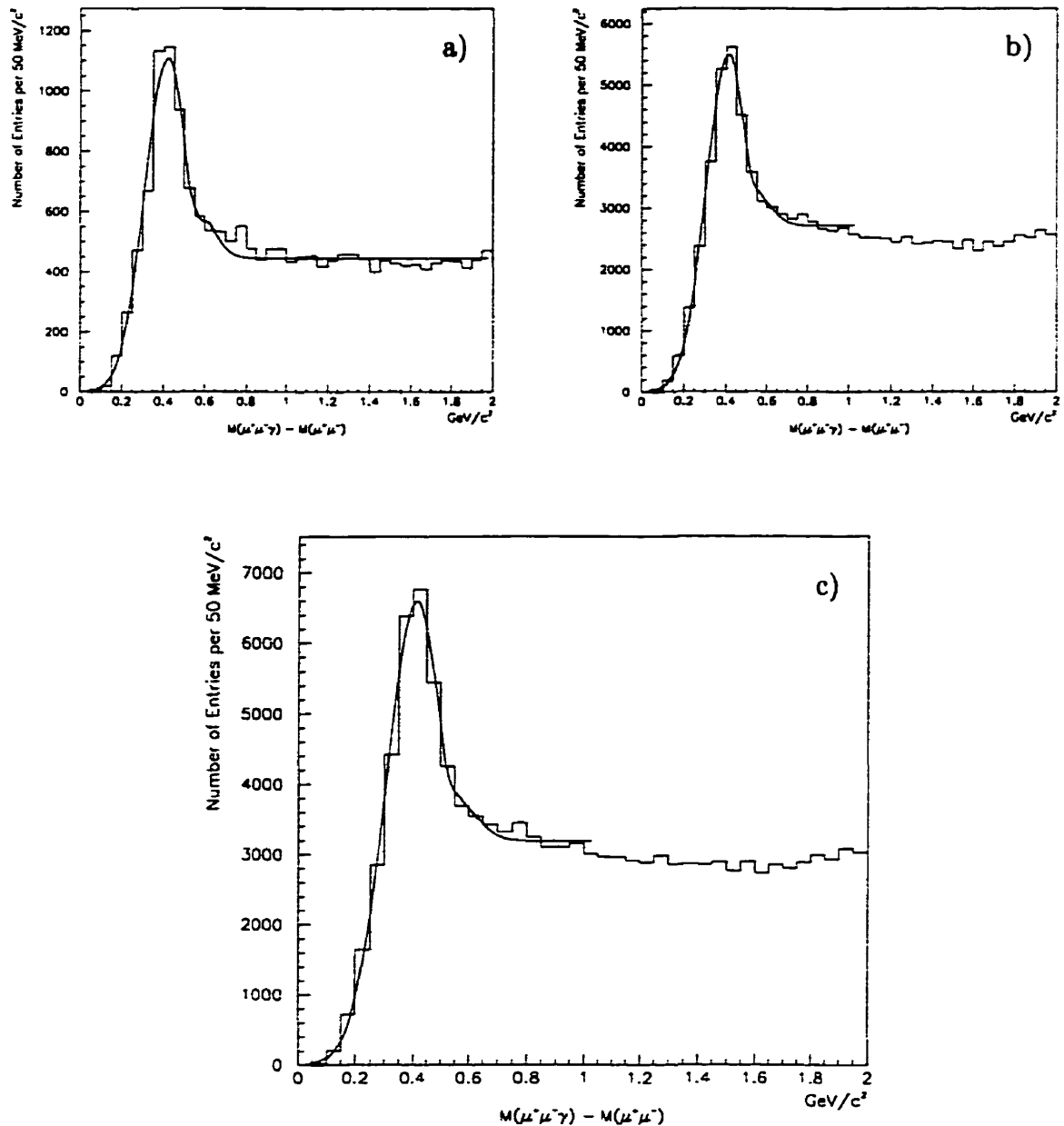


Figure 4.7: The  $\chi_c$  mass spectrum. Plot a) shows the  $\mu^+\mu^-\gamma$ ,  $\mu^+\mu^-$  mass difference distribution for the Run 1A sample, while b) and c) show the distribution for the Run 1B and total samples respectively.

#### 4.2.7 $B^\pm \rightarrow \chi_c K^\pm$ Reconstruction

All of the cuts on kinematical quantities of the  $B^\pm \rightarrow J/\psi K^\pm$  reconstruction are applied to this decay mode. An additional cut regarding the  $\chi_c$  mass

constraint was used:

- Probability of the photon satisfying the  $\chi_c$  mass constraint  $> 0.5\%$

Figure 4.8 shows the invariant mass distributions of the  $\chi_c K^\pm$  for the Run 1A and Run 1B as well as for the entire data sample. The gaussian function is not the result of a proper fit to the data but is merely a guide indicating the region where the  $B^\pm \rightarrow \chi_c K^\pm$  signal is expected to lie. Figure 4.9 shows the momentum distribution for the  $B^\pm \rightarrow \chi_c K^\pm$  candidates.

### 4.3 Summary of Reconstructed Decays

Three particle decays have been reconstructed in this analysis:  $J/\psi$ ,  $\chi_c$ , and  $B^\pm$ , with the  $B^\pm$  reconstructed via two decay modes. The mass spectra of these particles contain entries from true decays (signal) as well as combinatoric background entries. In order to determine the size of the signal (number of reconstructed true decays) the mass spectra were fit with a linear combination of functions which represented the signal and background. In the case of the  $J/\psi$  and the  $B^\pm \rightarrow J/\psi K^\pm$  decay mode the fitting function consisted of a sum of a gaussian and a first order polynomial. The gaussian represented the shape of the signal distribution while the first order polynomial represented the background. For the  $\chi_c$  mass distribution a gaussian was used to represent the shape of the signal, however, a polynomial was inadequate to describe the distribution of the background. Instead, a combination of a hyperbolic tangent and an exponential were used to describe the background region with masses less than and greater than the  $\chi_c$  mass peak respectively. Table 4.1 summarizes the results of the fits and table 4.2 compares the fit results with the world averages. Since the results of the fits were not used in the remainder of the thesis a thorough analysis of the systematic errors was omitted. The fit results

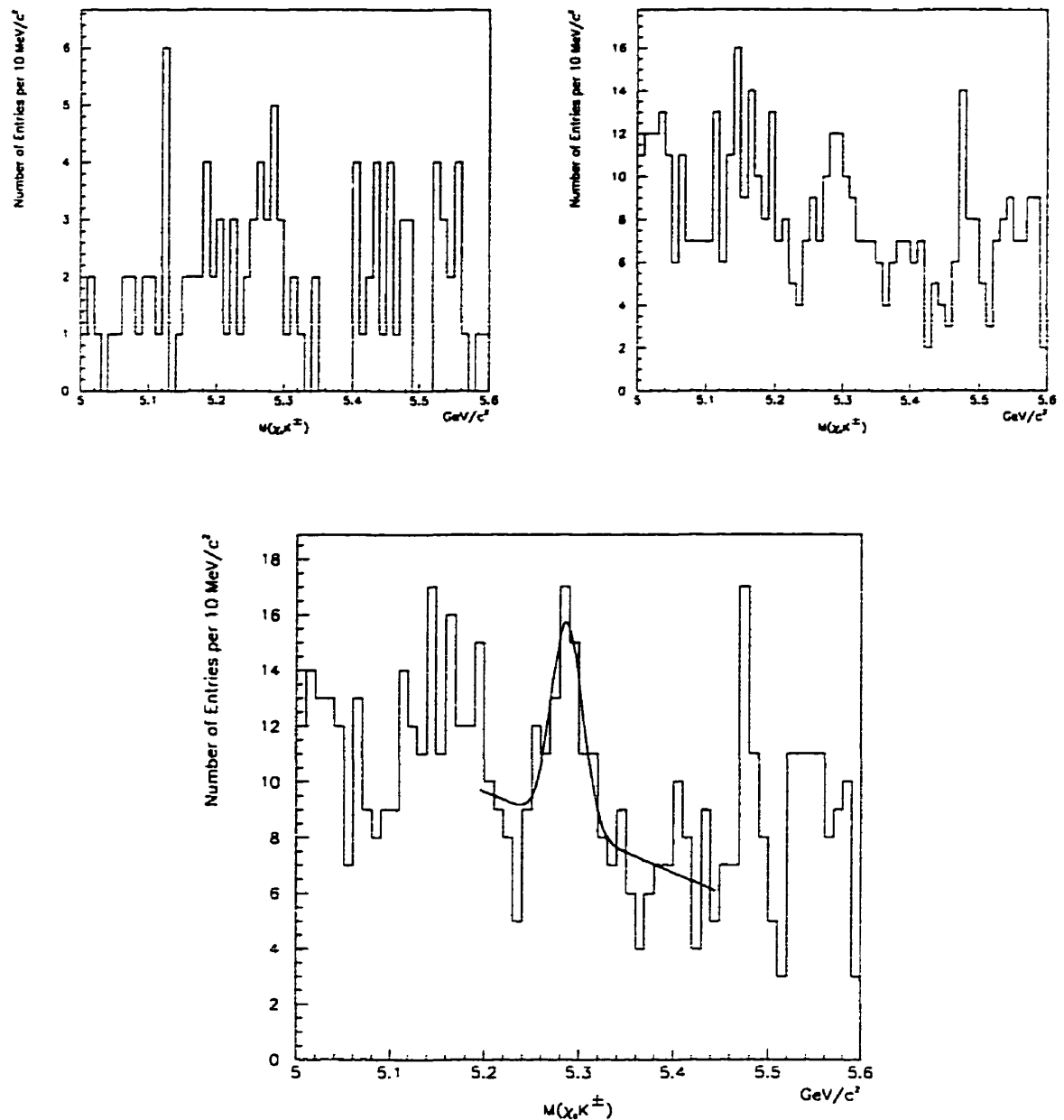
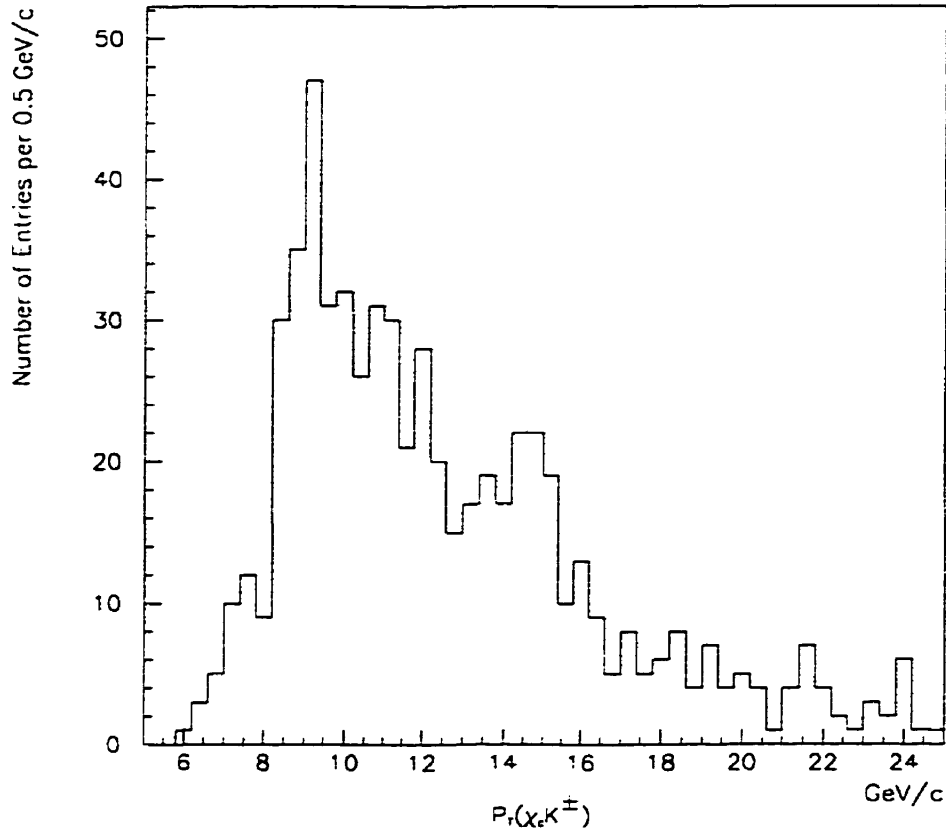


Figure 4.8: The  $\chi_c K^\pm$  invariant mass distribution. Plot a) shows the  $\chi_c K^\pm$  mass distribution for the Run 1A sample, while the b) and c) show the  $\chi_c K^\pm$  mass distribution for the Run 1B and total samples respectively.

are only used as a consistency check and the quoted errors are statistical only.

Figure 4.9: The  $P_T$  of the  $B$  candidates.

Decay	Number of Events	Mass ( $\text{GeV}/c^2$ )	$\sigma_M$ ( $\text{MeV}/c^2$ )
$J/\psi \rightarrow \mu^+ \mu^-$	$(3.015 \pm 0.015) \times 10^5$	$3.0958 \pm 0.0001$	$21.34 \pm 0.05$
$\chi_c \rightarrow J/\psi \gamma$	$35844 \pm 527$	$3.5098 \pm 0.0014$	$108.2 \pm 0.8$
$B^\pm \rightarrow J/\psi K^\pm$	$723 \pm 73$	$5.2778 \pm 0.0007$	$14.14 \pm 0.65$

Table 4.1: Summary of the decay reconstruction parameters for the total data sample. The values and errors quoted in this table are only the results of statistical fits to the data. They do not include systematic errors which are expected to be larger than the statistical ones.

Decay	$M_{Exp}$ (GeV/ $c^2$ )	$M_{Avg}$ (GeV/ $c^2$ )
$J/\psi \rightarrow \mu^+ \mu^-$	$3.0958 \pm 0.0001$	$3.09688 \pm 0.00004$
$\chi_c \rightarrow J/\psi \gamma$	$3.5098 \pm 0.0014$	$3.51053 \pm 0.00012$
$B^\pm \rightarrow J/\psi K^\pm$	$5.2778 \pm 0.0007$	$5.2787 \pm .0020$

Table 4.2: Comparison of the masses determined with this analysis ( $M_{Exp}$ ) with the global average values ( $M_{Avg}$ ).

## Chapter 5

# Relative Reconstruction Efficiency of the $B^\pm$ Decay Modes

Equation 4.3 expresses  $R$  as a function of  $N_{tot}(B^\pm \rightarrow \chi_c K^\pm)$  and  $N_{tot}(B^\pm \rightarrow J/\psi K^\pm)$ , the total number of decays of each process. What can be determined, however, is  $N(B^\pm \rightarrow \chi_c K^\pm)$  and  $N(B^\pm \rightarrow J/\psi K^\pm)$ , the total number of reconstructed decays for each decay mode. To determine  $N_{tot}$  the following is required:

- The number of reconstructed decays ( $N$ )
- The reconstruction efficiency for each decay channel ( $\epsilon_{rec}$ )
- The efficiency of each decay mode passing the trigger ( $\epsilon_{trigg}$ )

The total number of decays ( $N_{tot}$ ) is then given by:

$$N_{tot} = N / (\epsilon_{rec} \cdot \epsilon_{trigg}) \quad (5.1)$$

Therefore, the ratio of branching ratios is given by:

$$R = \frac{N(B^\pm \rightarrow \chi_c K^\pm)}{N(B^\pm \rightarrow J/\psi K^\pm)} \cdot \frac{\epsilon_{rec}^{J/\psi} \cdot \epsilon_{trigg}^{J/\psi}}{\epsilon_{rec}^{\chi_c} \cdot \epsilon_{trigg}^{\chi_c}} \quad (5.2)$$

where  $\epsilon^{J/\psi}$  and  $\epsilon^{\chi_c}$  refer to the efficiencies of the  $B^\pm \rightarrow J/\psi K^\pm$  and  $B^\pm \rightarrow \chi_c K^\pm$  decay modes respectively.

The number of reconstructed  $B^\pm \rightarrow J/\psi K^\pm$  decays are listed in table 4.1.  $\epsilon_{rec}$  and  $\epsilon_{trigg}$ , can be determined from Monte Carlo simulations of the decay kinematics and detector response. Efficiencies determined in such a manner, however, may contain systematic errors due to differences between actual detector response and the Monte Carlo modeling of said response as well as the differences between the Monte Carlo modeling of the  $B^\pm$  production mechanisms and the actual production mechanisms. Fortunately, since the two decay modes have certain efficiencies in common their cancellation will remove the source of systematic error entailed in the actual calculation of the efficiencies.

## 5.1 The Monte Carlo Simulation

The Monte Carlo program used in calculating the various efficiencies consisted of three main components: the event generation and decay component; the detector simulation component, and the event reconstruction component. Event generation uses a program called BGENERATOR [25] to generate  $b$  quarks according to the MRSD0 structure function with the mass of the  $b$  quark  $M_b = 4.75 \text{ GeV}/c^2$  and the  $\mu$  parameter set to  $\mu = \mu_0^1$  before hadronizing them into  $B^\pm$  mesons according to the Peterson fragmentation model [26]. The CLEOMC [27] program then decays the  $B^\pm$  mesons according to the desired decay modes with the proper kinematic behavior. The particles are then propagated through the various detector components by the CDFSIM program. CDFSIM fully simulates the detector's response according to the principles of interacting charged and neutral particles and the geometry and material of the detector. The calorimeter response, however, is not simulated

---

<sup>1</sup>The  $\mu$  parameter determines the absolute scale of quark production cross-section.  $\mu_0$  is the nominal value of the  $\mu$  parameter.

but is parametrized based on information from test beam data. The test beam data was collected for high energy particles and the response of the calorimeter was extrapolated to lower energies, such as the photon energies relevant to this analysis. This extrapolation is not believed to be accurate and hence, CDFSIM's simulation of the calorimeter response to low energy photons is not considered very reliable. Event reconstruction is then performed in the same manner as for data. The sole difference between the data and Monte Carlo event reconstruction algorithms lies in the treatment of the photons. Since it is desired to avoid using CDFSIM to simulate low energy photons the Monte Carlo event reconstruction algorithm uses the photon information from the CLEOMC program. The detector's response to these photons is determined separately from data and is described in section 5.3

## 5.2 $B^\pm$ Reconstruction Efficiencies

The reconstruction efficiency of the different decay modes can be broken down into several components due to the following sources:

- Incomplete spatial coverage of the detector
- Detector response
- Calibration and offline data processing
- Decay Reconstruction algorithms
- Kinematical cuts on the decay products

Although these components are listed and referred to individually they may not be independent of each other. Correlation between the various components have to be considered in order to correctly calculate the total efficiency.

Since the CTC and CEM only cover the region  $|\eta| < 1$ , any  $B^\pm$  decays in which the decay products lie outside this region will not be found by the event reconstruction algorithm. The component of the efficiency due to the incomplete spatial coverage of the detector relies as much on the spatial distribution of the  $B^\pm$  meson and their decay products as the fraction of the solid angle covered by the detector. The  $B^\pm$  spatial distributions are dependent on the production mechanism of the mesons and may not be accurately modeled in the Monte Carlo. This dependence, however, is diminished when the ratio of efficiencies of both decay modes is taken since the spatial distribution of the  $B^\pm$  will be the same for both decay modes. The spatial distributions of the  $B^\pm$  decay products, however, are not expected to be the same for the two decay modes. Hence, their contribution to the efficiency may not cancel when the ratio is taken, and will have to be determined. This, however, can be determined with good accuracy since the Monte Carlo can model the  $B^\pm$  decay product distributions well.

The contribution of the detector response and the offline data processing to the efficiency is based on the ability with which the various detector components and offline algorithms correctly identify and reconstruct the charged particle tracks and energy depositions of the  $B^\pm$  decay products. These terms are dependent on the  $P_T$  as well as the spatial distributions of the decay products. The  $P_T$  cuts imposed on the muons and kaons ensure that the particles lie in the range where their respective detector and reconstruction efficiencies have plateaued. This means that the component of the efficiencies due to detector response and reconstruction efficiencies of the charged tracks will be equal for both decay modes and will cancel when the ratio of efficiencies is taken. The component of the efficiency related to the photon reconstruction, however, remains to be evaluated. Since the efficiency due to the photon reconstruction is independent of the other components of the total efficiency it can be evaluated separately.

The components of the efficiency due to the decay reconstruction algorithms are related to the method with which the decay products are identified from the data and the way they are combined to reconstruct the  $B^\pm$  meson. The efficiency with which the decay products pass the mass, vertex, and pointing constraints are an example of the source of such efficiencies. With the exception of the photon, the reconstruction algorithms for both decay modes are identical and any efficiencies due to the particular decay reconstruction algorithm used will cancel when the ratio of efficiencies is taken.

Finally, the efficiency of the kinematical cuts reflects the probability of a  $B^\pm$  decay passing the various  $P_T$  cuts and the  $L_{XY}$  and isolation cuts. The efficiency due to the  $L_{XY}$  cut is equal for both decay modes since the decay time, and hence the distance travelled, of a particle is independent of the particle's decay mode. The efficiency of the isolation cut cannot be accurately determined from Monte Carlo since it requires a knowledge of the proton fragmentation mechanism in addition to the knowledge of the  $B^\pm$  production mechanism. However, since the isolation cut depends on the environment surrounding the  $B^\pm$  and not on the decay mode of the  $B^\pm$  the efficiencies of the isolation cut will be equal for the two decay modes and will cancel when the ratio is taken. The  $P_T$  cut efficiencies are related to the falling momentum spectrum of the  $B^\pm$  mesons. Since the momentum of a  $B^\pm$  meson is shared among more final state particles in the  $\chi_c$  decay mode the momenta of the charged particles will, on average, be less than that of the  $J/\psi$  decay mode charged particles. Consequently, requiring the same minimum  $P_T$  cuts on the  $K^\pm$ ,  $J/\psi$ , and the two muons is equivalent to higher  $P_T$  cuts on the  $B^\pm$  mesons which decay through the  $\chi_c$  mode which means that the  $P_T$  cuts will be less efficient for the  $\chi_c$  decay mode.

The efficiencies which do not cancel when the ratio of efficiencies is taken are listed below:

- The coverage term due to the spatial distribution of the  $B^\pm$  decay products.
- The  $P_T$  cuts term.
- All photon related terms.

The coverage and  $P_T$  cuts terms can be determined from Monte Carlo simulation, while the photon related terms are determined from data. The following sections describe how these efficiencies were determined and applied.

### 5.2.1 The $P_T(K^\pm)$ Cut Efficiency

It is expected that the  $P_T$  spectra of the  $K^\pm$  will be different for the two decay modes. Since the  $\chi_c$  is more massive than the  $J/\psi$ , energy and momentum conservation implies that the  $K^\pm$  from the  $\chi_c$  decay mode will be less energetic and will have a  $P_T$  spectrum peaked at lower momenta than that of the  $K^\pm$  from the  $J/\psi$  decay mode. The  $P_T$  spectra of the  $K^\pm$  from both decay modes is shown in figure 5.2 for the generated Monte Carlo  $B^\pm$   $P_T$  spectrum shown in figure 5.1. Imposing the minimum  $P_T(K^\pm)$  cut described in section 4.2.3 produces the  $B^\pm$   $P_T$  spectra shown in figure 5.3. Since the kaon momentum cut required  $K^\pm$  candidates with  $1.25 \text{ GeV}/c < P_T(K^\pm) < 2.0 \text{ GeV}/c$  to be SVX tracks the fraction of such tracks needed to be determined. This fraction, determined from data, was found to be independent of  $P_T$  in the range  $1.25 \text{ GeV}/c < P_T(K^\pm) < 2.0 \text{ GeV}/c$  and equal to  $0.53 \pm 0.02$ . This fraction was used as the weight of all events with  $1.25 \text{ GeV}/c < P_T(K^\pm) < 2.0 \text{ GeV}/c$  when applying the  $K^\pm$  momentum cut to the  $B^\pm$   $P_T$  spectrum. The ratio of the two  $P_T$  distributions produces the relative efficiency for a  $B^\pm \rightarrow \chi_c K^\pm$  decay to pass the kaon momentum cut with respect to that of a  $B^\pm \rightarrow J/\psi K^\pm$  decay passing the cut (Fig 5.4). The solid line in figure 5.4 is a result of fitting an exponential to the data points. An exponential function was used to fit the

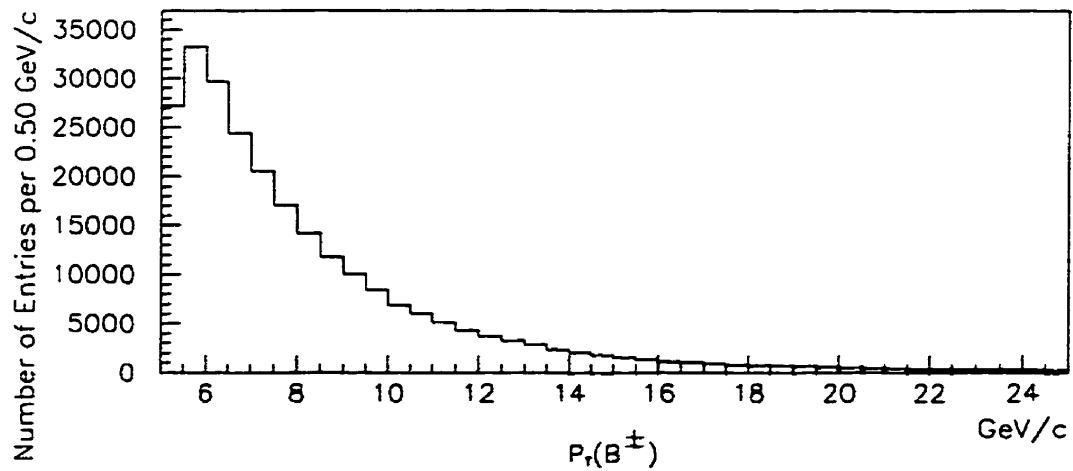


Figure 5.1: The Monte Carlo generated  $B^\pm$   $P_T$  spectrum.

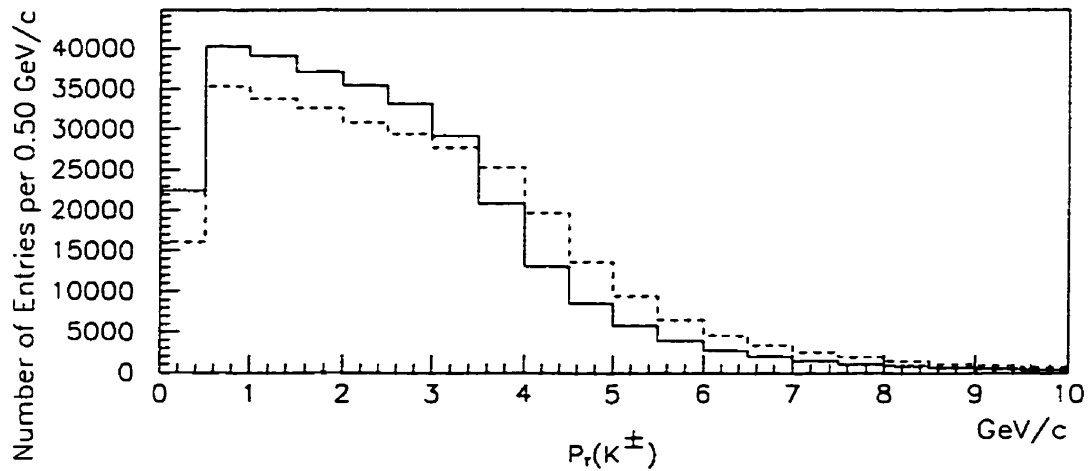


Figure 5.2: The Monte Carlo  $P_T$  spectra of the  $K^\pm$  from  $B^\pm$  decay. The solid line represents the  $K^\pm$  from the  $B^\pm \rightarrow \chi_c K^\pm$  decays while the dotted line represents the  $K^\pm$  from the  $B^\pm \rightarrow J/\psi K^\pm$  decays.

data points in the other efficiency plots as well since it matched the data well.

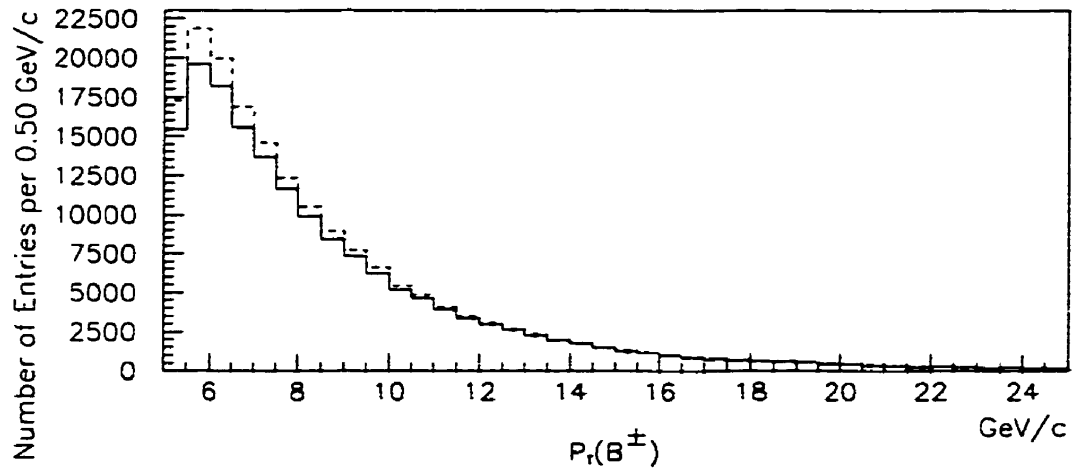


Figure 5.3:  $P_T$  spectra of the  $B^\pm$  with the  $K^\pm P_T$  cuts. The solid line represents the  $B^\pm \rightarrow \chi_c K^\pm$  decays while the dotted line represents the  $B^\pm \rightarrow J/\psi K^\pm$  decays.

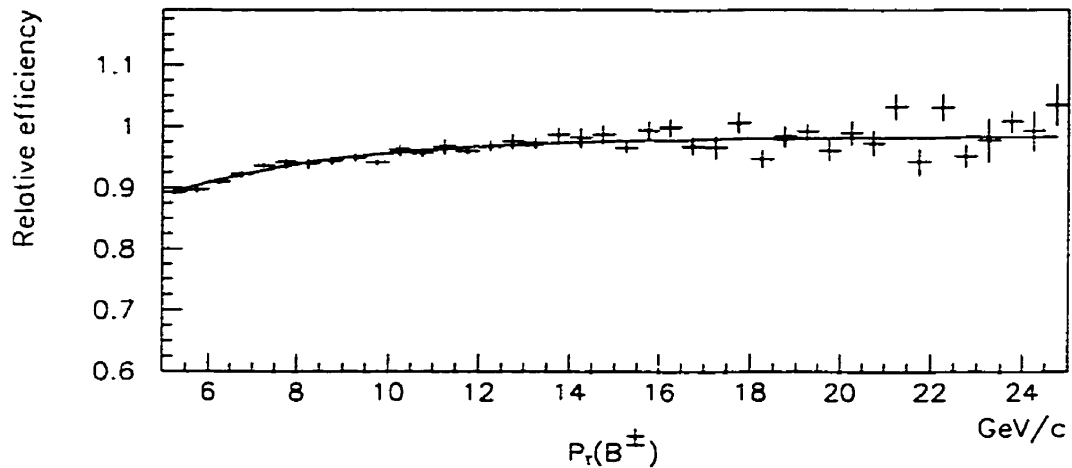


Figure 5.4: Efficiency of the  $K^\pm P_T$  cut, for the  $B^\pm \rightarrow \chi_c K^\pm$  decay mode with respect to the  $B^\pm \rightarrow J/\psi K^\pm$  decay mode, as a function of  $B^\pm P_T$

### 5.2.2 The $P_T(\mu)$ Cut and the Trigger Efficiency

Just as the  $P_T(K^\pm)$  spectra are different for the two decay modes, so are the  $P_T$  spectra of the two muons. The  $P_T$  spectra of the higher and lower

energy muons are shown in figures 5.5 and 5.6 respectively for the  $B^\pm$   $P_T$  spectrum shown in figure 5.1. Imposing the muon momentum cuts described

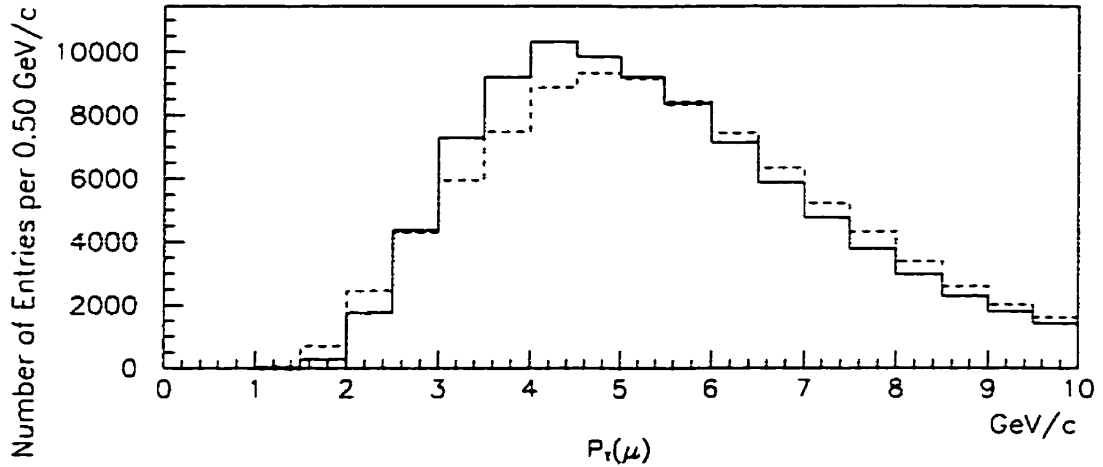


Figure 5.5: The Monte Carlo  $P_T$  spectra of the more energetic muon from the  $B^\pm$  decay. The solid line represents the muons from the  $B^\pm \rightarrow \chi_c K^\pm$  decay while the dotted line represents the muons from the  $B^\pm \rightarrow J/\psi K^\pm$  decay.

in section 4.2.1 produces the  $B^\pm$   $P_T$  spectra shown in figure 5.7, and the ratio of the two  $B^\pm$   $P_T$  distributions produces the relative efficiency of the  $P_T(\mu)$  cuts (Fig 5.8). The  $P_T(\mu)$  cuts ensure that the muons lie in the  $P_T$  range where the trigger efficiency has plateaued. Therefore,  $\epsilon_{trigg}^{\chi_c} / \epsilon_{trigg}^{J/\psi} = 1$ .

### 5.2.3 The $P_T(J/\psi)$ Cut

The  $P_T$  spectra of the  $J/\psi$  from both decay modes are shown in figure 5.9. Although the  $P_T(\mu)$  cuts and the  $P_T(J/\psi)$  cuts are highly correlated the relative efficiency of the  $P_T(J/\psi)$  cuts could still be different from 1. This efficiency is determined in two steps by generating the  $B^\pm$   $P_T$  spectra with only the  $P_T(\mu)$  cuts and then with both the muon and  $J/\psi$   $P_T$  cuts, for both decay modes. For each decay mode, the ratio of the  $P_T(B^\pm)$  spectrum with the two sets of

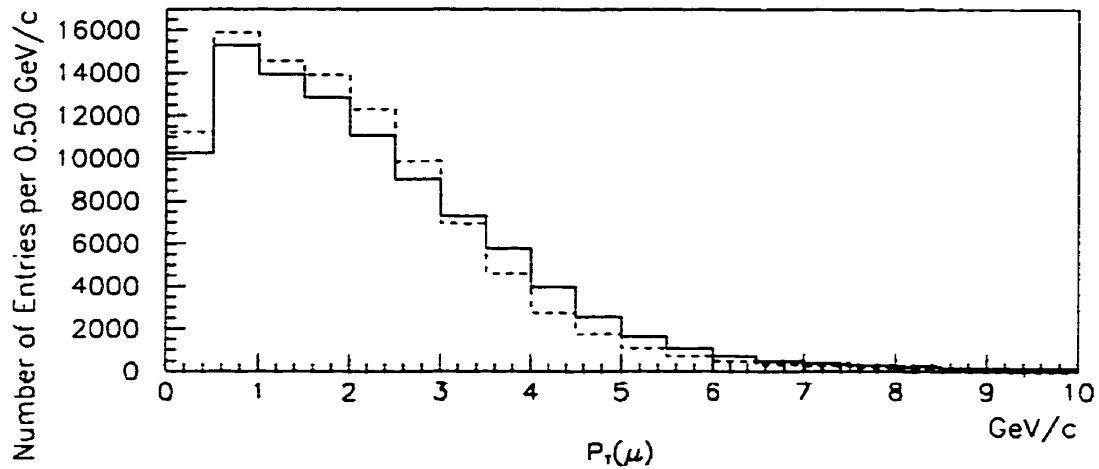


Figure 5.6: The Monte Carlo  $P_T$  spectra of the less energetic muon from the  $B^\pm$  decay. The solid line represents the muons from the  $B^\pm \rightarrow \chi_c K^\pm$  decay while the dotted line represents the muons from the  $B^\pm \rightarrow J/\psi K^\pm$  decay.

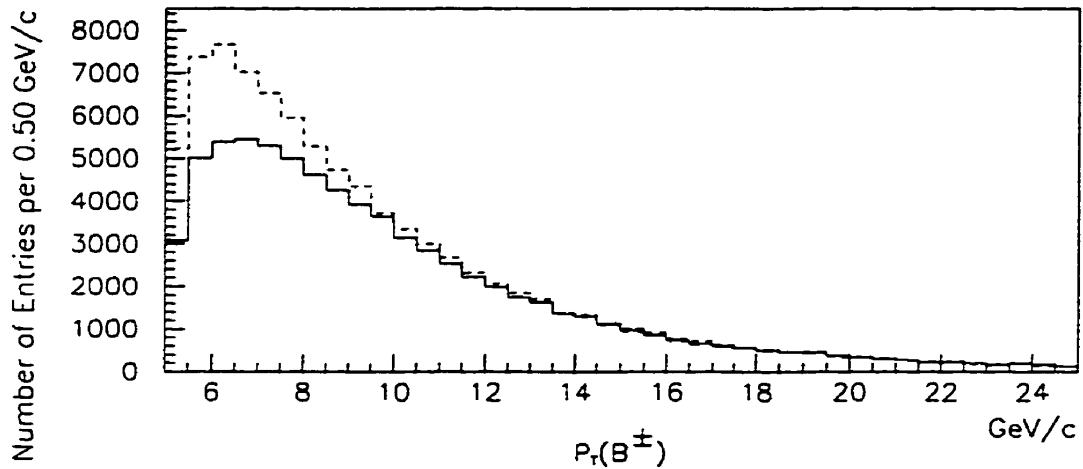


Figure 5.7:  $P_T$  spectra of the  $B^\pm$  with the muon  $P_T$  cuts. The solid line represents  $B^\pm \rightarrow \chi_c K^\pm$  decays while the dotted line represents  $B^\pm \rightarrow J/\psi K^\pm$  decays.

cuts with respect to the  $P_T(B^\pm)$  spectrum with only the  $P_T(\mu)$  cuts is taken. The ratio of the two resulting distributions is the relative efficiency for the

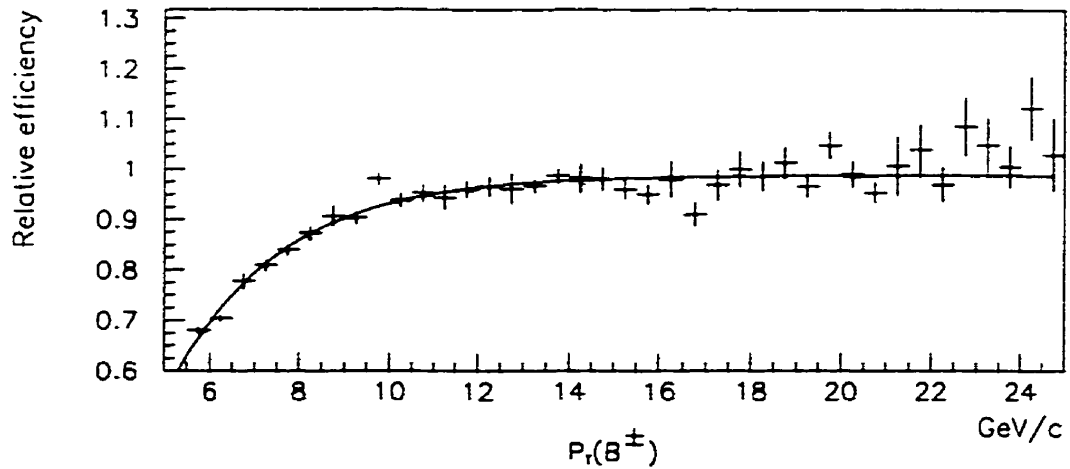


Figure 5.8: Efficiency of the muon  $P_T$  cuts, for the  $B^\pm \rightarrow \chi_c K^\pm$  decay mode with respect to the  $B^\pm \rightarrow J/\psi K^\pm$  decay mode, as a function of  $B^\pm P_T$

$P_T(J/\psi)$  cuts after the  $P_T(\mu)$  cuts have been imposed (Fig 5.10).

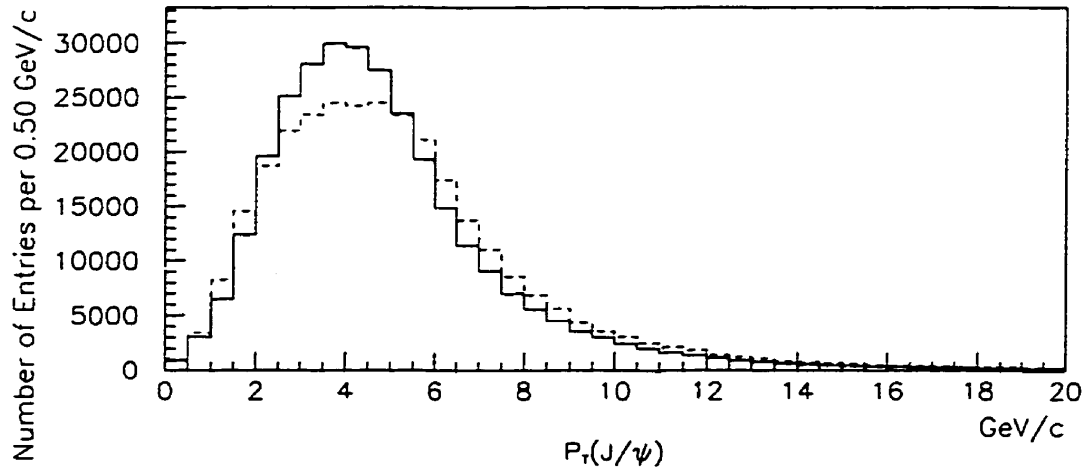


Figure 5.9: The Monte Carlo  $P_T$  spectra of the  $J/\psi$  from the  $B^\pm$  decay. The solid line represents the  $J/\psi$  from the  $B^\pm \rightarrow \chi_c K^\pm$  decay while the dotted line represents the  $J/\psi$  from the  $B^\pm \rightarrow J/\psi K^\pm$  decay.

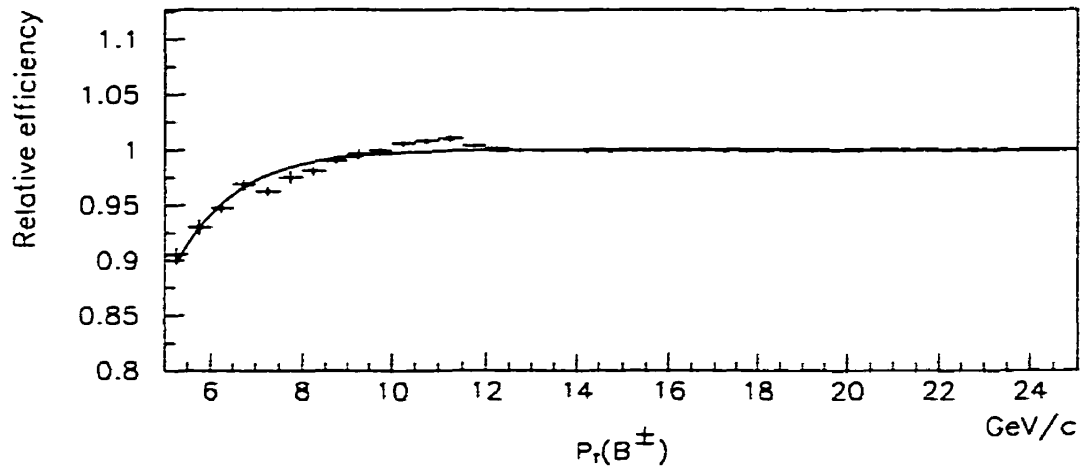


Figure 5.10: Efficiency of the  $J/\psi$   $P_T$  cuts, after the muon  $P_T$  have been imposed, as a function of  $B^\pm$   $P_T$

### 5.3 The Photon Reconstruction Efficiency

In principle, the photon reconstruction efficiency could be determined from Monte Carlo. This method is inadequate, however, in this case since the photons in question have energy on the order of 1 GeV while the detector photon response was studied with photons with energy larger than 10 GeV. Therefore, the detector response to low energy photons is not well understood and incorrectly modeled in the Monte Carlo.

The alternative would be to determine the photon reconstruction efficiency from experimental data. Since the calorimeter provides the only information about photons in an event, however, there is nothing against which the calorimeter response can be checked in order to determine the efficiency. Therefore, in order to determine the photon reconstruction efficiency from data one must use electrons. This is possible since the behaviour of electrons and photons in a calorimeter (i.e. electromagnetic showers) are identical. With

electrons, one has independent position and energy information from the reconstructed electron track in the CTC. Since the behaviour of muons, pions, kaons, and other charged particles in the calorimeter is very different from that of photons and electrons, one must be able to reliably identify electrons in the same energy range as the photons used in this analysis. The only way to reliably identify low energy electron tracks is through photon conversions. The  $0.08 X_0$  of material between the beam pipe and the inner wall of the CTC causes about 8% [28] of the photons to convert into electron-positron pairs. Hence, by reconstructing photon conversions one can obtain a very pure sample of electrons.

### 5.3.1 The Conversion electrons

All tracks in an event were assumed to be electrons or positrons<sup>2</sup> and were combined in pairs to form a photon if they satisfied the following requirements:

- $P_T$  of the track  $> 0.5 \text{ GeV}/c$ .
- The track extrapolated to a central calorimeter tower.
- The tracks were oppositely charged.

The track pairs were also required to satisfy a vertex constraint and a conversion constraint. The conversion constraint required that the two tracks be parallel at the point of intersection. This is kinematically equivalent to requiring that the invariant mass of the pair equal zero as is expected from the conversion of a massless photon. The small number of conversions found in the *dimuon* data sample did not allow for the determination of the photon reconstruction efficiency with sufficient statistical accuracy. Consequently, the

---

<sup>2</sup>Depending on the charge associated with the tracks. Subsequent mentions of electrons also refer to positrons.

high energy electron sample was used. This data sample was collected by a trigger which required an electron with energy  $E > 6$  GeV in the event. The energy range of electrons with  $E > 6$  GeV does not significantly overlap the energy range of the photons used in this analysis. However, if the high energy electron (positron) did actually originate from a photon conversion it is likely that the energy of the other conversion positron (electron) is lower, and thus falls in the relevant energy range.

Figure 5.11 shows the radial distribution of the conversion vertices in the  $r - \phi$  plane after the following cuts were applied.

- Probability of satisfying the vertex and conversion constraints  $> 0.1\%$ .
- Neither of the tracks associated with the conversion were SVX tracks.

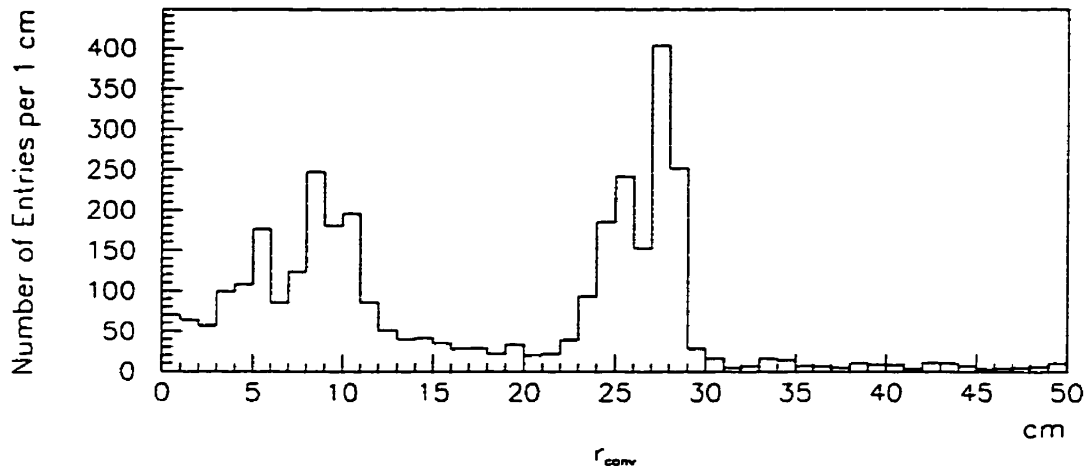


Figure 5.11: Radial distribution of the conversion vertices in the  $r - \phi$  plane.

The peaks at 25 cm and 28 cm are due to the conversions in the outer wall of the vertex tracking chamber and the inner wall of the CTC respectively. The series of peaks with radii less than 10 cm are due to conversions in the SVX and the surrounding support structures.

### 5.3.2 Determination of the Photon Reconstruction Efficiency

For the lower energy electron track from the selected conversion pairs an attempt is made to reconstruct a photon in the calorimeter tower to which the electron track extrapolates. Exactly the same criteria are applied as for the photon search in the analysis with the exception of the *no track* requirement<sup>3</sup>. Two distributions of the electron energy spectrum, as determined from the track momenta, are then created. The entries of the first distribution are all equally weighted, while the entries of the second distribution are weighted with 1 or 0 depending on whether or not a photon was reconstructed in the calorimeter tower (photon weighted) to which the electron track extrapolated. The ratio of the photon weighted distribution to the equally weighted one gives the photon reconstruction efficiency as a function of the actual photon energy (again without the *no track* requirement). Figures 5.12 and 5.13 show the electron energy distributions and the photon reconstruction efficiency respectively.

### 5.3.3 The 'No Track Cut' Efficiency

The no track requirement is used in the analysis in order to distinguish photons from electrons. It is possible however, that some tracks randomly extrapolated to the same calorimeter tower as the photon from the  $B$  meson decay. This would cause the photon to be rejected and the  $B$  meson not be reconstructed. In order to correct for this, one must determine how many photon candidates are being rejected due to the no track requirement.

Again, this can only be determined with electrons. This efficiency was determined in [29] with a sample of conversion electrons. Determination of the no

---

<sup>3</sup>Photon candidates were required to have no CTC track pointing at the tower within which they were reconstructed (section 4.2.5)

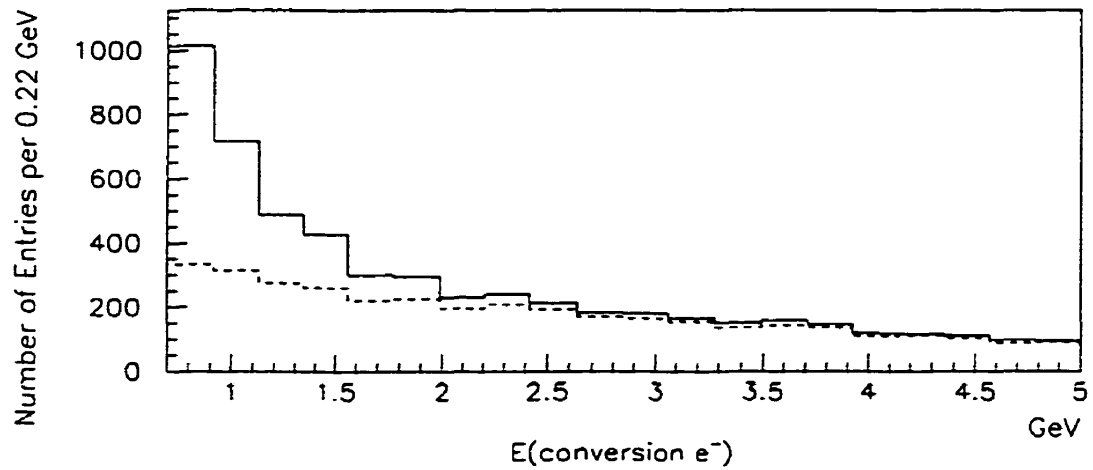


Figure 5.12: Energy distribution of conversion electrons. The solid histogram shows the equally weighted distribution and the dotted histogram shows the photon weighted distribution.

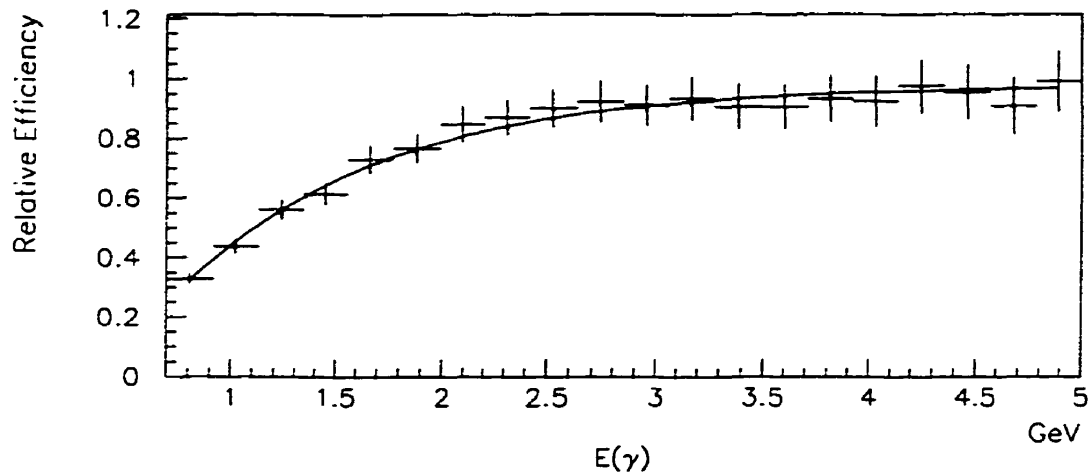


Figure 5.13: Photon reconstruction efficiency, without the *no track* cut, as a function of the photon's energy.

track requirement efficiency entailed identifying the calorimeter tower to which one of the conversion electrons extrapolated and counting the number of other tracks which extrapolated to the same tower. The efficiency was determined to

be  $\epsilon_{NoTrack}(\gamma) = 89^{+4}_{-5}\%$ . The reason that the value of  $\epsilon_{NoTrack}(\gamma)$ , determined with the *high energy electron* data sample, is applicable to the *dimuon* data sample is as follows: all the tracks associated with the  $B^\pm \rightarrow \chi_c K^\pm$  decay or the photon conversion are accounted for by the reconstruction algorithms. Therefore, any spurious tracks extrapolating to the same calorimeter tower as the photon (electron) must have originated from the underlying event, i.e. interactions not associated with the production of the  $B^\pm$  mesons (photon conversions). Such interactions are dependant on the instantaneous luminosity and are thus expected to occur with equal frequency in both the *dimuon* and the *high energy electron* data samples.

### 5.3.4 The ‘Photon Fiducial Volume Cut’ Efficiency

A fiducial volume cut of  $|x_{wedge}| < 20$  cm,  $|z_{wedge}| > 10$  cm was applied to all photon candidates. The purpose of this cut was to ensure that the energy depositions were sufficiently far from the calorimeter towers’ edge that the amount of *unmeasured* energy is minimized. The fiducial volume cut eliminates 21.2% of the surface area of the calorimeter, hence its contribution to the efficiency is  $\epsilon_{fid-vol}(\gamma) = 78.8\%$ . The total photon reconstruction efficiency is the product of the three photon efficiency terms.

## 5.4 The Total Relative Efficiency

The kaon, muon,  $J/\psi$  and photon efficiencies were fitted with the following function:  $A_1 + \exp(-A_2(x - A_3))$  where the  $A_i$  were the fit parameters. For  $\epsilon(K^\pm)$ ,  $\epsilon(\mu)$ , and  $\epsilon(J/\psi)$ ,  $x$  is the  $P_T$  of the  $B^\pm$ . For  $\epsilon(\gamma)$ , however,  $x$  is the energy of the photon. Multiplying them together to determine the total relative efficiency is, strictly, incorrect since there may be some correlations between the kaon,  $J/\psi$ , and photon efficiencies. Correlations between the muon and

$J/\psi$  efficiencies were accounted for in the creation of  $\epsilon(J/\psi)$ . Combining the efficiencies together with the proper correlation produces the total relative efficiency  $\epsilon'(P_T(B^\pm), E(\gamma))$ , which is a function of the  $P_T$  of the  $B^\pm$  and the energy of the photon.  $\epsilon'(P_T(B^\pm))$  and the abovementioned correlations have been determined by using the Monte Carlo with all the aforementioned cuts applied. Equation 5.2 then reduces to:

$$R = \frac{N(B^\pm \rightarrow \chi_c K^\pm)}{N(B^\pm \rightarrow J/\psi K^\pm)} \cdot \frac{1}{\epsilon'(P_T(B^\pm), E(\gamma))} \quad (5.3)$$

$R$  is then determined by dividing the ratio of reconstructed decays, as a function of  $P_T(B^\pm)$  and  $E(\gamma)$ , by the total relative efficiency.

## 5.5 Systematic Errors

The systematic errors on the relative reconstruction efficiency were evaluated in the same fashion as the efficiency itself. The fit parameters ( $A_i$ ) of the various efficiency functions were varied by  $\pm 1\sigma$  and  $\epsilon'$  and  $R$  recalculated. The difference between the central value of  $R$  and the two extremes is taken to be the systematic error.

# Chapter 6

## Results and Conclusions

It can be seen from figure 4.5 that  $B^\pm \rightarrow J/\psi K^\pm$  decays have been reconstructed from the CDF data. For the case of the  $B^\pm \rightarrow \chi_c K^\pm$  decay, a peak can be seen at the approximate mass of the  $B^\pm$  (Fig 4.8). Prior to claiming a  $B^\pm \rightarrow \chi_c K^\pm$  signal, the following studies were performed to determine the signal's robustness. The stability and significance of the peak, however, have not been conclusively established due to some apparent self-inconsistencies.

The data was divided into three sub-samples: the Run 1A data, the first 60% of the Run 1B data (Run 1B <sub>$\alpha$</sub> ), and the final 40% of the Run 1B data (Run 1B <sub>$\beta$</sub> ). The Run 1B data were divided in that manner to correspond to a hiatus in the data-taking. The three sub-samples corresponded to an integrated luminosity of 19, 55, and 35 pb<sup>-1</sup> respectively. Figure 6.1 shows the reconstructed  $\chi_c K^\pm$  mass spectra for the three sub-samples. A peak is more readily seen in the Run 1B <sub>$\alpha$</sub>  plot. Run 1B <sub>$\alpha$</sub> , however, is the sub-sample with the largest integrated luminosity. In order to determine the behaviour of the  $\chi_c K^\pm$  peak as a function of integrated luminosity each distribution was fit to the sum of a Gaussian and a first order polynomial. The width of the gaussian was fixed to the value determined from a Monte Carlo simulation of  $B^\pm \rightarrow \chi_c K^\pm$  decays;  $\sigma_{MC} = 0.012$  GeV/ $c^2$ . This is done to allow the

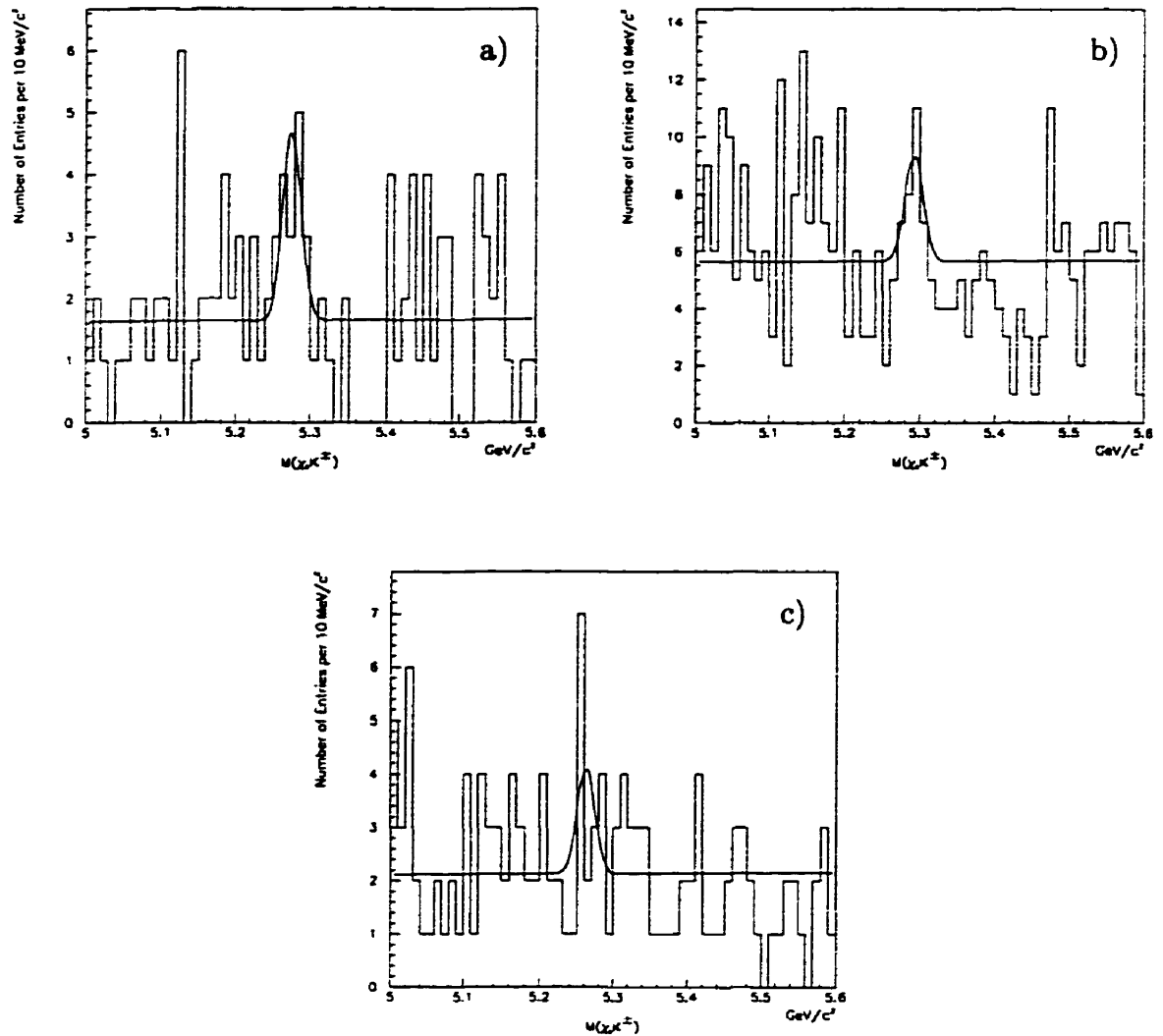


Figure 6.1: The invariant mass distribution of the  $B^\pm \rightarrow \chi_c K^\pm$  candidates in the three data sub-samples. Plot (a) is the Run 1A  $\chi_c K^\pm$  mass distribution while plots (b) and (c) are for Run 1B $_\alpha$  and Run 1B $_\beta$  respectively.

comparison of the entries in the  $\chi_c K^\pm$  peak, between the three sub-samples. The results of these fits are summarized in Table 6.1. The number of entries in the  $\chi_c K^\pm$  peak ( $B^\pm$  yield), and its error, for each sample were scaled to an integrated luminosity of  $10 \text{ pb}^{-1}$  to allow for a comparison of the  $B^\pm$  yield. The scaled  $B^\pm$  yield for Run 1B $_\alpha$  and Run 1B $_\beta$  are both quite smaller than

	Run 1A	Run 1B <sub><math>\alpha</math></sub>	Run 1B <sub><math>\beta</math></sub>
Mass( $B^\pm$ )	$5.276 \pm 0.008$	$5.292 \pm 0.008$	$5.262 \pm 0.010$
Number of $B^\pm$	$9.2 \pm 4.3$	$11.2 \pm 6.1$	$6.0 \pm 4.1$
$B^\pm$ per 10 pb <sup>-1</sup>	$4.84 \pm 2.26$	$2.04 \pm 1.11$	$1.71 \pm 1.17$
Ratio of luminosities	1	2.89	1.84

Table 6.1: Comparison of the  $\chi_c K^\pm$  mass fit results for the three data subsamples. The entries of the third row are the results of scaling the values number of  $B^\pm$  to an integrated luminosity of 10 pb<sup>-1</sup>.

the value obtained for Run 1A, however, they are not totally self-inconsistent since their errors are quite large too. The location of the peaks, however, in both the Run 1B <sub>$\alpha$</sub>  and Run 1B <sub>$\beta$</sub>  distributions are more than  $1\sigma$  away from the mass of the  $B^\pm$  meson ( $M_{B^\pm} = 5.279 \text{ GeV}/c^2$ ). This is indicative of a possible inconsistency between the three data samples.

Comparison of other kinematical quantities reveals more inconsistencies between the Run 1A and Run 1B data. Figure 6.2 compares the  $J/\psi$ ,  $\chi_c$ , and  $B^\pm \rightarrow \chi_c K^\pm$  candidate mass distributions as well as the isolation ( $\text{Isol}(\chi_c K^\pm)$ ) distribution between the Run 1A sample and the total Run 1B sample. The distributions have been normalized to one in order to compare their shapes. It can be seen in figure 6.2(a) that the signal-to-background ratio for the  $J/\psi$  and  $\chi_c$  distributions has deteriorated from Run 1A to Run 1B. It can also be seen that the isolation of the  $B^\pm$  candidates has noticeably decreased. Both these effects might be explained by the higher instantaneous luminosity in Run 1B. The lower signal-to-background ratio in the  $J/\psi$  and  $\chi_c$  distributions may explain an increased level of background in the  $\chi_c K^\pm$  mass distribution but they cannot account for a diminution of the  $B^\pm \rightarrow \chi_c K^\pm$  signal. The isolation cut, however, will reject more  $B^\pm \rightarrow \chi_c K^\pm$  candidates in Run 1B than in Run 1A since they are less isolated. It is not expected that this effect will substantially deteriorate the signal, However, time limitations did not permit for it to be studied in more detail.

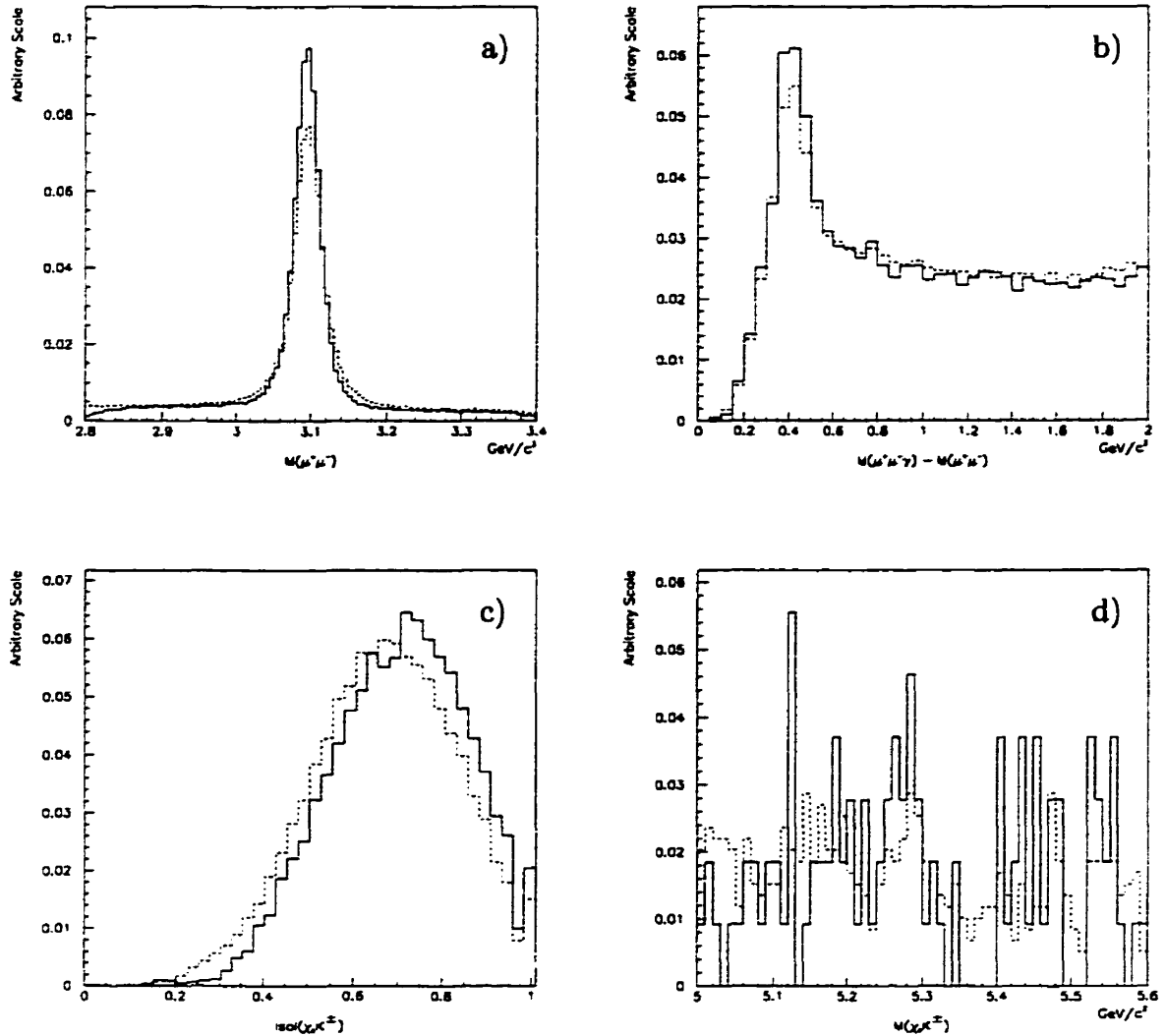


Figure 6.2: Comparison of the  $\mu^+\mu^-$  (a),  $\mu^+\mu^-\gamma - \mu^+\mu^-$  (b), and  $\chi_c K^\pm$  (c) mass distributions as well as the  $\chi_c K^\pm$  isolation, between the Run 1A and Run 1B data samples. The solid histograms represent the Run 1A data while the dashed histograms represent the Run 1B data.

A comparison of the data between the two Run 1B sub-samples was also performed in an attempt to further understand the discrepancies in the  $\chi_c K^\pm$  mass distributions. Figure 6.3 compares the photon energies between the Run 1B $_\alpha$  and Run 1B $_\beta$  samples, as well as the  $\mu^+\mu^-$ ,  $J/\psi\gamma$ ,  $J/\psi K^\pm$ , and  $\chi_c K^\pm$  mass

distributions and the isolation of the  $\chi_c K^\pm$ . On average, the photons in Run 1B $_\beta$  are slightly less energetic than those in Run 1B $_\alpha$ . A fraction of the low energy depositions in the calorimeter, especially around and below 1 GeV, is due to calorimeter noise. A photon energy distribution that is shifted towards lower energies implies that it contains more entries due to calorimeter noise and is a possible indication of a deterioration in the calorimeter performance. The isolation distribution of the Run 1B $_\beta$  sub-sample is shifted towards lower values. This effect is explained by the increasing instantaneous luminosity, but is not believed to account for a smaller than expected  $B^\pm \rightarrow \chi_c K^\pm$  yield. The  $\mu^+ \mu^-$ ,  $J/\psi \gamma$ , and  $J/\psi K^\pm$  mass distributions exhibit a lower signal-to-background ratio in the Run 1B $_\beta$  sub-sample. These effects contribute to the background of the  $\chi_c K^\pm$  distribution as described above. The location of the  $J/\psi$  mass peak, however, is shifted slightly towards lower mass in the Run 1B $_\beta$  sub-sample. This may indicate that our knowledge of the solenoidal magnetic field is incorrect in one of the sub-samples. An incorrect value of the solenoidal magnetic field could slightly shift the  $\chi_c K^\pm$  mass on an event by event basis and may result in a shifted and possibly wider signal peak. The shift in the  $\chi_c K^\pm$  mass is a consequence of the systematic error of the  $K^\pm$  momenta since the  $J/\psi$  candidates are mass constrained. It is important to note, however, that since the unconstrained  $J/\psi$  candidate mass is shifted from its nominal value, the efficiency of such candidates passing the mass constraint requirement is decreased, resulting in fewer  $B^\pm \rightarrow \chi_c K^\pm$  candidates. This is qualitatively consistent with the shift towards lower (higher) masses of the  $\chi_c K^\pm$  peak in the Run 1B $_\beta$  (Run 1B $_\alpha$ ) data, as seen in Figure 6.1 and Table 6.1

Despite the lack of a strong  $B^\pm \rightarrow \chi_c K^\pm$  signal in the Run 1A and Run 1B data, it is believed that the  $\chi_c K^\pm$  mass distribution contains entries from  $B^\pm \rightarrow \chi_c K^\pm$  decays. Requiring stricter kinematic cuts, such as the muon and kaon  $P_T$  cuts, the photon energy, the isolation and  $L_{X\gamma}$  cuts

eliminates a large fraction of the  $B^\pm \rightarrow \chi_c K^\pm$  candidates; the remaining candidates, however, lie around  $M = 5.278 \text{ GeV}/c^2$  and are consistent with originating from  $B^\pm \rightarrow \chi_c K^\pm$  decays. The remaining events, however, are too few to enable a meaningful measurement of the ratio of branching ratios ( $R = \frac{\mathcal{B.R.}(B^\pm \rightarrow \chi_c K^\pm)}{\mathcal{B.R.}(B^\pm \rightarrow J/\psi K^\pm)}$ ).

The differences between the three data sub-samples are partially explained by the changes in the instantaneous luminosity and the detector performance over the course of the experiment. Such effects require further study in order to determine whether a conclusive  $B^\pm \rightarrow \chi_c K^\pm$  signal can be extracted from the CDF data, and are beyond the scope of this thesis. Further investigation of these effects, however, holds promise that the  $B^\pm \rightarrow \chi_c K^\pm$  signal can be conclusively established and the ratio  $R$  determined from the CDF data. The CDF experiment has demonstrated that  $B$  physics can be successfully studied within the hadronic environments of  $p\bar{p}$  collisions; this analysis has shown that exclusive decays of  $B^\pm$  mesons ( $B^\pm \rightarrow J/\psi K^\pm$ ) can be reconstructed within that environment, and has hinted that even *complex* decay modes involving four final state particles with low energy photons can be fruitfully investigated.

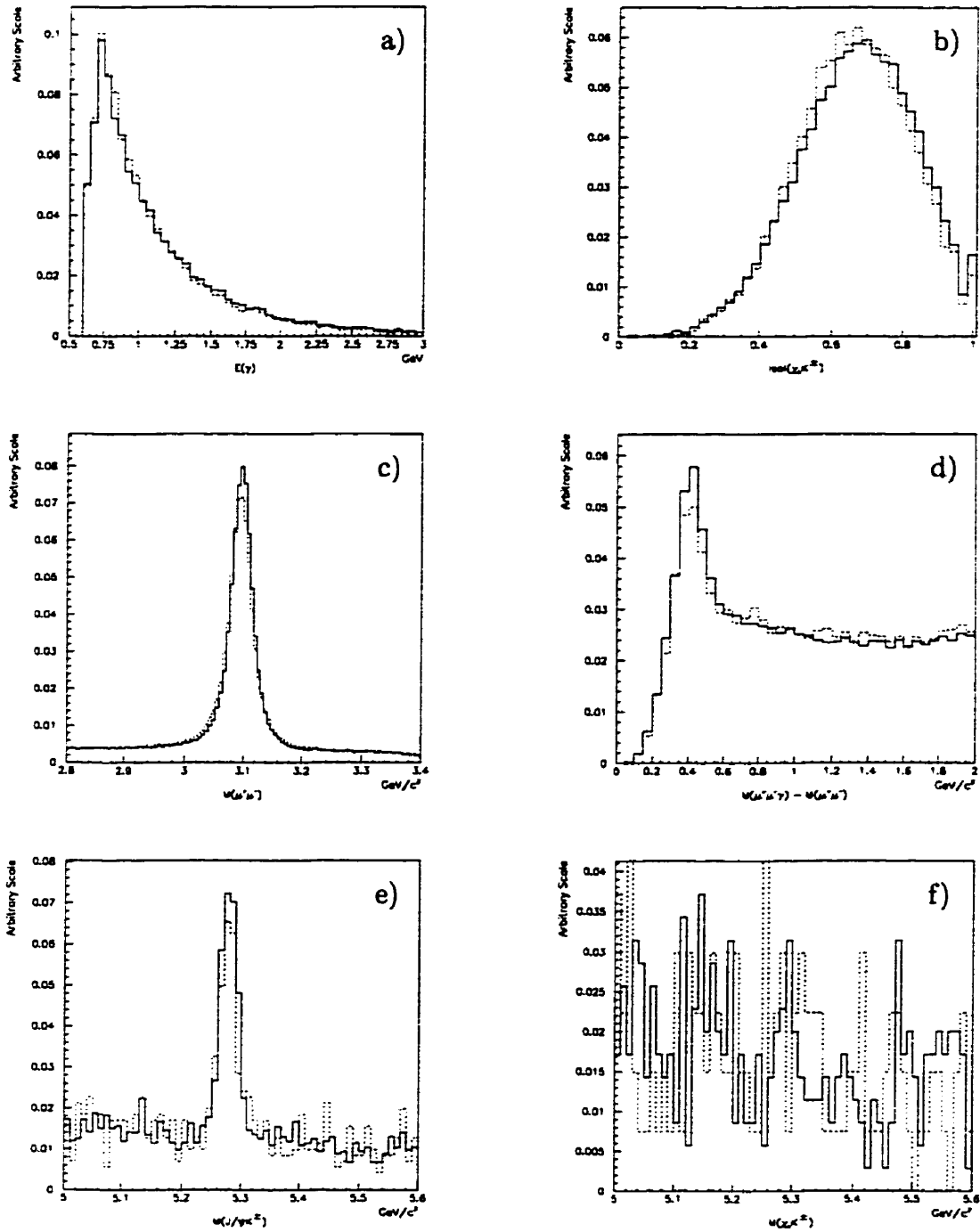


Figure 6.3: Comparison of the photon energies (a), isolation of the  $\chi_c K^\pm$  (b), and the  $\mu^+\mu^-$  (c),  $\mu^+\mu^-\gamma - \mu^+\mu^-$  (d),  $J/\psi K^\pm$  (e), and  $\chi_c K^\pm$  (f) mass distributions, between the Run 1B<sub>α</sub> and Run 1B<sub>β</sub> data. The solid histograms represent the Run 1B<sub>α</sub> data while the dashed histograms represent Run 1B<sub>β</sub>.

# Bibliography

- [1] G. Preparata. Predictions for the top quark mass and for the generalized Cabibo angle. *Phys. Lett.*, 82B:398, 1979.
- [2] The CDF collaboration. Observation of top quark production in  $p\bar{p}$  collisions with the Collider Detector at Fermilab. *Phys. Rev. Lett.*, 74:2626–2631, 1995.
- [3] J.D. Bjorken and S.D. Drell. *Relativistic Quantum Fields*. McGraw-Hill, 1965.
- [4] D. Griffiths. *Introduction to Elementary Particles*. John Wiley, 1987.
- [5] L. Montanet *et al.* The Particle Data Group. Review of particle physics. *Phys. Rev.*, D50:1173, 1994.
- [6] S. L. Glashow. Partial symmetries of weak interactions. *Nucl. Phys.*, 22:579, 1961.
- [7] A. Salam. Electromagnetic and weak interactions. *Phys. Lett.*, 13:168–171, 1964.
- [8] S. Weinberg. A model of leptons. *Phys. Rev. Lett.*, 19:1264–1266, 1967.
- [9] F. Wilczek. unknown. *Ann. Rev. Nucl. Sci.*, 32:177, 1982.
- [10] M. Kobayashi and T. Maskawa. CP violation in the renormalizable theory of weak interaction. *Prog. Theor. Phys.*, 49:652–657, 1973.

- [11] G.P. Lepage G.T. Boduri, E. Braaten. Non relativistic QCD. *Phys. Rev.*, D51:1125, 1995.
- [12] A.B. Santra A. N. Kamal. Probing factorization in color suppressed  $B \rightarrow \psi(2S)K(K^*)$  decay. *Phys. Rev.*, D51:1415, 1995.
- [13] The CDF collaboration. Measurement of the B meson differential cross section in  $p\bar{p}$  collisions at  $\sqrt{s} = 1.8$  TeV. *Phys. Rev. Lett.*, 75:1451–1455, 1995.
- [14] The CDF collaboration. Measurement of  $\sigma \cdot B(W \rightarrow e\nu)$  and  $\sigma \cdot B(Z^0 \rightarrow e^+e^-)$  in  $p\bar{p}$  collisions at  $\sqrt{s} = 1.8$  TeV. *Phys. Rev. Lett.*, 76:3070–3075, 1996.
- [15] The CDF collaboration. Measurement of the mass of the  $B_S^0$  meson. *Phys. Rev.*, D53:3496–3505, 1995.
- [16] The CDF collaboration. Measurement of the  $B^+$  and  $B^0$  meson lifetimes. *Phys. Rev. Lett.*, 72:3456–3460, 1994.
- [17] The CDF collaboration. Reconstruction of  $B^0 \rightarrow J/\psi K_S^0$  and measurement of ratios of branching ratios involving  $B \rightarrow J/\psi K^{(*)}$ . *Phys. Rev. Lett.*, 76:2015–2020, 1996.
- [18] D. Amidei *et. al.* The silicon vertex detector of the Collider Detector at Fermilab. *Nucl. Inst. and Meth.*, A350:73–130, 1994.
- [19] F. Bedeschi *et. al.* Design and construction of the CDF central tracking chamber. *Nucl. Inst. and Meth.*, A268:50–74, 1988.
- [20] M. Atac *et. al.* Measurement of drift velocities and lorentz angles at 15 kG. *Nucl. Inst. and Meth.*, A249:265–276, 1986.
- [21] The CDF collaboration. The CDF detector: An overview. *Nucl. Inst. and Meth.*, A271:387–403, 1988.

- [22] G. Ascoli *et al.* CDF central muon detector. *Nucl. Inst. and Meth.*, A268:33–40, 1988.
- [23] The CDF collaboration. *The CDF II Detector : Technical Design Report.* Fermilab, 1997.
- [24] M. Shapiro. *The YBOS Reference Manual*, 1988.
- [25] Paris Sphicas. A  $b\bar{b}$  monte carlo generator. CDF Note No. 2655, 1994.
- [26] C. Peterson *et al.* *Phys. Rev.*, D27:105, 1993.
- [27] P. Avery J. Lewis. CLEOMC: The CDF Interface to the CLEO Monte Carlo (QQ). CDF Note No. 2724, 1994.
- [28] A. B. Wicklund. Determination of the CDF inner detector material using conversion electrons. CDF Note No. 2899, 1994.
- [29] The CDF collaboration. Production of  $J/\psi$  from  $\chi_c$  decays at CDF. *Phys. Rev. Lett.*, 68:33–40, 1988.